AEROELASTIC STABILITY OF CANTILEVERED PLATES WITH INTERNAL CONSTRAINTS IN SUBSONIC POTENTIAL FLOW

by

BENJAMIN KEITH MORRIS

(Under the Direction of R. Benjamin Davis)

ABSTRACT

Landing gear doors on aircraft have experienced flutter during preliminary flight testing. While designs vary widely, landing gear doors are typically plate-like structures with a relatively rigid actuator attached to their inside surface. To better understand the aeroelasticity of landing gear doors, this study investigates the aeroelastic stability of an idealized model. The model consists of a hinged plate with an interior constraint approximating the actuator attachment. The plate is subject to uniform flow, and an unsteady vortex lattice model is coupled to the structural model to predict critical flow velocities. The location and footprint area of the internal constraint, along with plate aspect and mass ratios, are varied to investigate a large parameter space. Results reveal that the critical flow speed and instability mechanism are sensitive to the postulated actuator placement. In general, flutter is the dominant mode of instability when the actuator is postulated in the leading quarter of the plate. In other postulated locations, divergence dominates. However, the exact shape and location of the boundary between flutter and divergence is configuration dependent and found to be especially sensitive to changes in aspect ratio.

INDEX WORDS: aircraft, structural dynamics, aeroelasticity, vortex lattice, landing gear

AEROELASTIC STABILITY OF CANTILEVERED PLATES WITH INTERNAL CONSTRAINTS IN SUBSONIC POTENTIAL FLOW

by

BENJAMIN KEITH MORRIS

B.S., The University of Georgia, 2018

A Thesis Submitted to the Graduate Faculty of The University of Georgia in Partial Fulfillment of the Requirements for the Degree

MASTER OF SCIENCE

ATHENS, GEORGIA

2020

AEROELASTIC STABILITY OF CANTILEVERED PLATES WITH INTERNAL CONSTRAINTS IN SUBSONIC POTENTIAL FLOW

by

BENJAMIN KEITH MORRIS

Major Professor: R. Benjamin Davis

Committee: C. Brock Woodson
Eric C. Freeman

Electronic Version Approved:

Ron Walcott
Interim Dean of the Graduate School
The University of Georgia
May 2020

Acknowledgements

Completing this research has been one of the most challenging and rewarding experiences of my life. Writing this thesis required me to draw on all of my academic knowledge from both my formal and informal training to this point, and I often needed help to push through various challenges. I would like to thank my mentors, peers, and family for supporting me and challenging me to be the best I can be.

I would like to thank my advisor, Dr. Davis, for always making himself available for assistance and for elevating my standards for excellence. I am grateful for the guidance of my advisory committee members, Dr. Woodson and Dr. Freeman. I am grateful for the support of my labmates, especially Eetu Kohtanen, who was instrumental in helping me learn the details of the vortex lattice method. I would like to acknowledge the GAIN fellowship sponsored by the graduate school, which provided me with funding through my graduate studies. I'd also like to thank my parents for their unyielding support and for always smiling and nodding while I told them about the details of my work. Lastly, I'd like to thank my life partner Enid for her unwavering support. She always keeps me inspired and motivated.

Contents

List of Tables

List of Figures

Nomenclature

Roman Symbols

A Plate surface area

A_f Fixed node footprint area

a Spanwise length of the plate

b Chordwise length of the plate

$[C1], [C2]$ Fluid forcing matrices (Eq.(2.25))

$[D1], [D2]$ State-space structural matrices (Eq. (2.25))

D Flexural rigidity

E Young's modulus

f Natural frequency

H Aspect ratio of the plate, a/b

h Thickness of the plate

$[K]$ Stiffness matrix (Eq.(2.5))

k Influence coefficient

L Lagrangian

$[M]$ Mass matrix (Eq.(2.5))

n Time step number

n_s Total number of structural mesh elements

P Pressure

Q Generalized force

q Modal coordinate

r_1, r_2 State-space coordinates

$\mathcal{T}$ Total kinetic energy

Δt Time step size

t Time

U Free-stream velocity

U_{cr} Critical free-stream velocity

U^*_{cr} Reduced critical free-stream velocity

$\mathcal{V}$ Total potential energy

W_1 First column of mesh in the wake

W_d Plate / downwash velocity

w Out-of-plane displacement

$\Delta x, \Delta y$ Chordwise / spanwise length of pinned region

$\delta x, \delta y$ Chordwise / spanwise length of VLM mesh element

x, y Cartesian coordinates

x_a Chordwise position of finite-length vortex filament

y_a, y_b Spanwise position of lower / upper vortex filament

Greek Symbols

$[\beta]$ Downwash matrix (Eq.(2.25))

Γ Vortex strength

Λ Discrete-time eigenvalue

λ Continuous-time eigenvalue

μ Mass ratio

ν Poisson's ratio

$\hat{\phi}$ Structural mode shape

ϕ Fluid velocity potential

$[\psi]$ Structural Ritz vector matrix

$[\tilde{\Theta}_q]$ Aeroelastic mode shape matrix

Ψ Ritz vector

ρ_f Fluid density

ρ_s Structural density

$[\sigma], [\xi]$ Influence coefficient matrices (Eq.(2.25))

$[\tilde{\Theta}_R], [\tilde{\Theta}_L]$ Real aeroelastic mode shape matrices

$\bar{\mathbf{\Theta}}$ Aeroelastic eigenvector

$\bar{\mathbf{\Theta}}_L$ Left eigenvector

$[\tilde{\xi}], [\tilde{\eta}]$ Aeroelastic modal coordinates

$\hat{\zeta}$ Normalized damping

ζ Damping ratio

Super/Subscripts

i, j Indices (Eq. (3.2))

r, c Row / column indices for wake elements

Chapter 1

Introduction and Background

It should be noted that much of the content of this thesis is taken directly from the author's original research article submission [1]. Before discussing the fine details of the aeroelastic model and results, it is useful to present several topics that will add perspective to the present work. First, the typical features of landing gear doors are discussed. Second, the literature on aeroelastic models of landing gear doors and similar systems is presented and discussed. Finally, an overview of panel methods focusing on methods suitable for lifting surface analysis is presented to lend insight into the properties of each method.

1.1 Landing Gear Doors

Although not present on all winged aircraft, landing gear doors are a common feature in airplane design. Landing gear doors are typically thin, flexible structures that cover the landing gear during flight. The doors are opened during takeoff and landing to allow the landing gear to be deployed. While the exact geometry of landing gear doors varies across aircraft designs, they are typically plate-like structures with a hinge at one edge and a relatively rigid actuator installed somewhere on the interior surface of the door. Figure 1.1 shows two examples of landing gear doors from two different manufacturers. Note that the actuator in 1.1a is mounted near the leading edge while the actuator in 1.1b is mounted near the trailing edge.

(a) (b)

Figure 1.1. Examples of landing gear doors on (a) a Gulfstream G650 (front view, reproduced from [2]), and (b) a Boeing 727 (front view, reproduced from [3])

Landing gear doors on aircraft have experienced flutter during flight testing [4]. According to the Federal Aviation Regulations Parts 23 and 25, aircraft must be completely free of any type of aeroelastic instability [5, 6]. However, the aeroelastic behavior of typical landing gear doors has not been widely studied. The aspect ratio of the door and the location of the actuator are common design parameters, but there is currently no published guidance on how these parameters influence the aeroelastic stability of landing gear doors. The ability to quickly estimate the aeroelastic behavior of a design without the use of detailed modeling techniques enables aircraft engineers to identify the potential for aeroeslatic instability early in the design process, thus preventing costly redesigns. Here, we intend to address this by considering the aeroelasticity of an idealized landing gear door model.

1.2 Plates with Internal Boundary Conditions

The aeroelastic stability of airfoils is typically discussed in terms of flutter and divergence. Flutter is a type of instability during which the airfoil experiences unbounded, harmonic motion. The vibrational amplitude of the structure increases exponentially with time. Divergence is a type of instability characterized by a loss of structural stiffness and an unbounded displacement of the airfoil. The flutter or divergence velocity of the structure is the lowest free-stream velocity at which the structure experiences flutter or divergence, respectively. Few studies have directly considered the aeroelastic stability of landing gear doors. Blades and Cornish [4] conducted one such study in which they used fully coupled finite element and computational fluid dynamics models to predict the critical flutter speeds of a landing gear door with fixed geometry and subject to different sideslip angles and flow speeds. They were able to match stability data from flight

tests with a few different values of sideslip angle and velocity. The analysis informed a redesign of the door which stiffened the door and satisfied the necessary stability criteria. A similar study by Tomac et al. [7] investigated the aerodynamics of aircraft landing gear using a hybrid Reynolds-averaged Navier-Stokes/large eddy simulation (RANS-LES) technique. The researchers intend to use the results to inform a vibration mitigation effort on the aircraft. Despite the accuracy of these methods, they are computationally expensive and provide little insight into how design changes may influence aeroelastic stability.

In an attempt to further increase accuracy and reduce computational costs, some studies have investigated landing gear doors through hybrid experimental-numerical approaches. Abarca et al. [8] used wind tunnel data to construct a fluid loading model based on principles of random response analysis. The wind tunnel data was used to construct a cross-spectral pressure matrix that was used to predict aerodynamic loading on a finite element structural model of a landing gear door. The hybrid model was validated with flight test data. The model inherits mathematical rigor and reproducibility from the structure while retaining the physical accuracy and detail from the experimental fluid measurements. However, because the fluid model is introduced to the structure as a simple load, only one-way coupling is achieved. Schwochow et al. [9] performed an operational modal analysis of a landing gear door in flight. Using the stochastic subspace identification method (SSI), they were able to extract modal information from the door under operating conditions. The experimental method automatically accounts for all kinds of aerodynamic loading and likely provides the most accurate estimates of aeroelastic modal properties. However, given the expense of flight testing, and the fact it does not result in predictive models, the utility of the method is limited.

The acoustic noise generated by landing gear assemblies has been studied extensively [10–15]. Fattah et al. [16] studied the aeroacoustics of a simplified landing gear door with an actuator strut. The model consisted of a rigid flat plate and cylinder in a uniform flow field, and CFD calculations were performed using a standard finite-volume solution of the Navier-Stokes equations. Results showed that the presence of the cylinder can have significant effects on the system's acoustic pressure. However, the far-field effects of the cylinder appear to decrease quickly with the distance from the plate to the surface of the cylinder.

While few studies have investigated the stability of landing gear doors themselves, there are many studies that investigate variations of flat plates under aerodynamic loading. Since the structure is the primary element of interest in these studies, and since the variations to the standard flat plate model typically serve to modify the mass, stiffness, or aerodynamic properties of the structure, the present work on landing gear

doors may be considered a part of a larger class of research on modified flat plates in external flow. Hence, it is useful to consider these related works since they may expose similar trends to those present in the dynamics of landing gear doors.

When an aircraft wing is damaged by a projectile, the resulting hole modifies the fluid-structure interaction by changing the fluid boundary condition on the wing's interior. Conyers et al. [17, 18] numerically and experimentally studied the aeroelasticity of flat plates with holes. Using the doublet lattice method, they found that flutter velocity is proportional to the damaged structure's natural frequency. Their results showed that the addition of a hole near the wing tip might significantly stabilize the nominal flutter mode, thus increasing the plate's flutter velocity. Similar experimental studies on the effects of ballistic damage to helicopter rotors showed that damage to the rotors causes a decrease in lift and an increase in drag [19]. The increase in drag results in an increase in flutter velocity and a decrease in divergence velocity [20]. Therefore, there exists a critical amount of damage at which the divergence velocity drops below the flutter velocity, making divergence the dominant mode of instability [20]. Other studies have investigated the stability behavior of aircraft wings with wing stores [21–23]. External stores used to carry missiles are common components of military aircraft. Tang et al. [21] models the wing store as an added mass attached to the wing via an added stiffness at the attachment point. Using the vortex lattice method (VLM), they found that the flutter velocity is significantly increased when the store is located at approximately 50% span. They also found that the location of the store significantly affects the wing's natural frequencies.

1.3 Vibration of Plates

A plate is a flat structure with a thickness much smaller than its width or length. Due to the small thickness, all quantities may be assumed to be constant through the plate's thickness, reducing the problem to two dimensions along the width and length. A comprehensive review of modal analysis of plates is given by Leissa [24]. Many of the structural equations presented in the present work are taken from Leissa's report.

There are several mathematical descriptions of structural plates, but the Kirchoff-Love theory of thin plates (also called "classical plate theory") [25] and the Mindlin-Reissner theory for thick plates [26] are the most commonly used. Kirchoff-Love plate theory is the extension of Euler-Bernoulli beam theory to two dimensions, and many of the same limitations apply to both theories. The primary assumption of both classical beam and plate theory is that planar cross sections remain planar. Hence, the vibration amplitude

must be small and there must be minimal local rotation. The Mindlin-Reissner theory accounts for the rotational inertia and shear stresses present in thick plates, allowing for plate theory to be extended to thicker elements without resorting to the use of the general theory of solids. However, thick plate theory is still much more complicated than thin plate theory, so Kirchoff-Love is still the most commonly used when applicable.

While analytical solutions exist for some simple geometries and boundary conditions, the classical plate equations do not in general have a closed-form solution. Approximations for the natural frequencies and mode shapes of rectangular plates with edge boundary conditions were first offered by Warburton, who used products of beam mode shapes in the span and chordwise directions as an input basis for Rayleigh's method [27]. Warburton's approximations were suitable for any combination of boundary conditions, but lost accuracy for high-order mode shapes [24]. Another set of simpler approximations was later proposed by Janich, who also employed Rayleigh's method but used trigonometric functions as a basis [28]. Janich's approximations were less accurate than Warburton's and were unsuitable for some boundary conditions, but their formulation was much simpler [24].

Modern solution of the classical plate equation is typically accomplished via finite element analysis (FEA) software. FEA results are themselves approximations, but they typically far surpass the required level of accuracy of a given problem. Furthermore, FEA formulations may be used to solve the plate equation for plates with arbitrary planar geometry and boundary conditions. In contrast to classical methods like Rayleigh's method, FEA allows boundary conditions to lie on the interior of the domain. However, the robustness of FEA may come at the cost of intuition. The approximations of Warburton and Janich, while limited in their applicability, were elegant in that any plate mode shape could be readily described and notated as a product of either beam mode shapes or sinusoids. While the low-order modes of complicated systems solved via FEA may still often be loosely referenced as "bending" or "torsional" modes, it is typically difficult to describe high-order modes without visualization.

1.4 Fluid Models

The following discussion draws heavily from the discussions in Ref. [29]. Note that while an enormous body of research is dedicated to microscopic flows, only macroscopic flows relevant to the present work are discussed here.

1.4.1 Overview of Fluid Theories

A general continuous medium may be represented by the five fundamental balance laws, so-called conservation of mass, conservation of linear momentum, conservation of angular momentum, conservation of energy, and the entropy inequality. These laws, together with the appropriate set of constitutive relationships and boundary conditions are sufficient to model any classical continuous system. In this sense, fluid systems differ from solid systems only in the constitutive relationships. If the pressure and density of a fluid system do not depend appreciably on temperature, the system may be fully described using only the laws of conservation of mass and momentum. In a fluid context, conservation of mass is represented by the continuity equation while conservation of momentum is represented by the Navier-Stokes equations. These four equations are generally accepted as a complete, yet complicated, representation of fluid mechanics.

The Navier-Stokes equations may be simplified under certain assumptions about the constitutive relationships. If the fluid is Newtonian (viscosity is not a function of strain rate) and viscosity is constant through the domain, the viscous terms of the Navier-Stokes equations simplify greatly. If the fluid is also inviscid, the equations further reduce to the Euler equations. Note that for incompressible flow the Euler equations simplify greatly, and the set of incompressible Euler equations is commonly referred to as just "the Euler equations". Adding the assumptions that the flow is irrotational and incompressible results in a simple fluid model known as "ideal" or "potential" flow. Potential flow is described by Laplace's equation, a linear differential equation. Hence, Laplace's equation may be satisfied by any superposition of known solutions, provided the solutions satisfy the boundary conditions.

1.4.2 Navier-Stokes Solvers

Until the 1950s and the advent of scientific computing, the Navier-Stokes equations saw limited use in engineering applications due to their complexity. Between the 1950s and the end of the century, several researchers began developing and implementing computational fluid dynamics (CFD) algorithms. By the turn of the century, the use of CFD codes in engineering design was ubiquitous.

Navier-Stokes and other similar CFD solvers traditionally employ finite-difference methods where the equations are discretized, a meshed grid of solution points is generated, and the equations are solved at each grid point. The discretization and grid generation schemes must be chosen carefully, since a poor discretization can easily lead to an unstable algorithm [29]. Implicit discretizations such as Crank-Nicolson are

commonly used for their improved stability [30]. Alternatively, the Navier-Stokes equations may be solved via a finite element approach. Indeed, many modern commercial FEA packages support fluid modeling.

The general form of the Navier-Stokes equations includes time derivatives, which enable the solution of unsteady flow problems. Algorithms that solve the general, unsteady form of the equations are often called "unsteady" or "time-accurate" CFD algorithms. For steady flow, the time-varying terms may be neglected, resulting in a set of equations that vary only in space. Algorithms that solve the steady form of the Navier-Stokes equations are often called "steady" CFD algorithms. While steady algorithms are computationally efficient, they are only suitable for simple flows where turbulence is negligible. Unsteady algorithms are typically required to study complicated flows where turbulence must be modeled. Steady algorithms may also only be applied to static or quasi-static structural problems where one-way coupling is assumed. If the motion of the elastic structure is expected to significantly modify the behavior of the fluid, an unsteady algorithm must be used to account for two-way coupling.

Due to their accuracy, Navier-Stokes solvers are frequently used to study systems with complicated geometry or turbulent flow regimes where high resolution is required. The method may also be modified to garner additional insight from a system. The Reynolds averaged Navier-Stokes (RANS) equations represent a time average of the flow [31]. The method results in a mean component representing the global evolution of the flow and a fluctuating component representing turbulent fluctuations. The two components together represent the total flow in a more understandable way. RANS models are time-averaged, so they do not directly model turbulence. An eddy viscosity term is added to the equations to approximate turbulent effects. A similar method known as large eddy simulation (LES) aims to reduce the computational costs of traditional Navier-Stokes solvers by ignoring small length scales [32]. This is accomplished by applying a low-pass filter to the Navier-Stokes equations [33]. In this way, turbulent flows may be resolved more efficiently than by direct numerical simulation at the cost of high-frequency detail. While RANS and LES are ultimately similar methods, RANS approaches the problem of data reduction statistically while LES uses a filtering approach. LES is often more computationally expensive than RANS because LES models large length scale turbulence while RANS only models the mean flow and includes turbulent effects through lower-order modeling. Hybrid RANS-LES methods have recently been developed to unite the two approaches, and a review of hybrid methodologies is available [34].

1.4.3 Panel Methods

While Navier-Stokes CFD solvers allow for arbitrary geometry and are highly accurate, they are computationally expensive. For circumstances where only a low-order approximation of fluid behavior is required, extreme accuracy can be sacrificed for computational efficiency. If irrotational, inviscid, incompressible flow may be assumed, a class of simple models known as panel methods may be derived based on potential flow. These methods are well suited to external flow problems where the effects of the fluid on a structure are of primary interest.

Under the assumptions of potential flow, the Navier-Stokes equation reduces to Laplace's equation. Laplace's equation is associated with a number of elementary solutions (such as sources, vortices, and doublets) that are presented in most advanced fluid mechanics and aerodynamics texts [29, 35, 36]. These solutions may be superposed to create a new solution satisfying a set of boundary conditions. The principle of superposition, which is valid for linear systems, is therefore the foundation of all potential flow panel methods.

A panel method begins by meshing the surface of the structure and an appropriate region in its wake with a finite number of panel elements. Each panel has associated with it an elementary solution with an unknown strength and a collocation point where a boundary condition is to be enforced. Since the assumed solutions are elementary solutions, Laplace's equation is automatically satisfied, and we are left with a system of equations representing the boundary conditions in terms of the unknown strengths. The equations are then solved, yielding a solution that satisfies the fluid equations of motion and the boundary conditions.

There are a few typical boundary conditions associated with panel methods [29]. Solution points on the structure are typically associated with tangency conditions, wherein the component of flow normal to the solid surface must be zero. Solution points in the wake are typically associated with convection conditions, which state that the elemental solutions must move at the free-stream velocity. Finally, points at the interface of the structure and the wake enforce the Kutta condition [36], which states that there must be no circulation at the trailing edge. Other boundary conditions such as the "recovery of conditions at infinity" condition may be applied to some systems.

The simplest panel method uses point source solutions, where the element strength represents the volume flow rate from the source [36]. While the mathematical formulation for this panel method is simple and it is

able to accurately capture the effects of a solid body on a fluid flow by the use of no-through-flow boundary conditions, the symmetry of the element equations means it cannot accurately calculate lift on an airfoil [35]. Hence, panel methods using point sources are not widely used.

The two most widely used panel methods for calculations on lifting surfaces are the doublet lattice method (DLM) and vortex lattice method (VLM), which employ doublet and vortex elementary solutions, respectively. The DLM is a robust method that has been applied extensively to study lifting surfaces including high-aspect ratio rectangular wings [37], delta wings [37, 38], T-tail aircraft [39], and rectangular wings with internal holes [17, 18]. Conyers provides a detailed description of the DLM in his dissertation [18]. The most difficult technical challenge associated with the DLM is the calculation of the kernel function, which relates the doublet strength to the induced velocity at all points in space. This is not a trivial task, since the calculation involves the evaluation of a singular integral [18]. The evaluation of this integral has been studied and improved by several researchers [40–42].

The VLM, while slightly less flexible than the DLM, is still widely used. A detailed description of the VLM is given in Gibbs' thesis [43]. A review of applications is available for the interested reader [44]. The VLM is a standard tool for airfoil analysis and has been used to study low aspect-ratio rectangular plates [45], rectangular plates with a variety of boundary conditions [43, 46–48], and limit cycle oscillations of rectangular and delta wings [21, 22, 49–51]. The elementary solution used for the VLM is a horseshoe vortex constructed from a finite-length, spanwise-oriented vortex filament connecting two semi-infinite vortex filaments that extend infinitely into the wake. Unlike the kernel function for doublet elements, the kernel function that relates the horseshoe vortex strength to the downwash velocity is an algebraic expression that may be easily calculated for each element, making the VLM more computationally efficient. Furthermore, reduced-order methods have been developed to optimize efficiency [52–54]. However, the DLM is slightly more flexible than the VLM. In contrast to the VLM's horseshoe vortex elements, the DLM's doublets are geometrically finite, so geometries with self-intersecting wakes (e.g., wings with holes, propellers) may be accurately analyzed. Fortunately, recent work has extended the VLM to overcome this and other limitations [55–58]. For a geometry in steady flow that does not generate a self-intersecting wake, the DLM and VLM are identical [18].

Chapter 2

Numerical Model

The aeroelastic model consists of an unsteady VLM coupled to a linearly elastic plate. This model has been thoroughly described elsewhere (see, e.g., Refs. [43,45,47,59]), and the details are discussed in the following sections. The plate is assumed to have isotropic material properties and undergo small displacement. The fluid model is based on incompressible potential-flow (irrotational, inviscid) theory.

2.1 Structural Model

The out-of-plane displacement of the plate, w, is assumed to take the form of a sum of Ritz vectors, Ψ, multiplied by generalized coordinates

$$w(x,y,t) = \sum_{j}^{\infty} \Psi_j(x,y) q_j(t), \tag{2.1}$$

where x and y are spatial coordinates, t is time, and q_j are generalized coordinates. Discretizing the domain at a finite number of collocation points transforms Eq. (2.1) into a matrix equation,

$$\boldsymbol{w} = [\psi]\boldsymbol{q}(t), \tag{2.2}$$

where $[\psi]$ is a matrix of Ritz vectors. As shown by several authors [24, 43, 45, 60], the kinetic energy $\mathcal{T}$ and potential energy $\mathcal{V}$ of the plate are given by

$$\mathcal{T} = \frac{1}{2}\rho_s h \int_A \left(\frac{\partial w}{\partial t}\right)^2 dA, \tag{2.3}$$

$$\mathcal{V} = \frac{D}{2}\int_A \left(\left(\frac{\partial^2 w}{\partial x^2}\right)^2 + \left(\frac{\partial^2 w}{\partial y^2}\right)^2 + 2\nu\left(\frac{\partial^2 w}{\partial x^2}\frac{\partial^2 w}{\partial y^2}\right) + 2(1-\nu)\left(\frac{\partial^2 w}{\partial x \partial y}\right)^2 \right) dA, \tag{2.4}$$

where ρ_s is the structural density, h is the plate thickness, and A is the plate surface area. The symbol D denotes flexural rigidity and is defined by $D = Eh^3/12(1-\nu^2)$, where E is Young's modulus, and ν is Poisson's ratio. An application of Lagrange's equation yields the familiar equations of motion,

$$[M]\ddot{\boldsymbol{q}}(t) + [K]\boldsymbol{q}(t) = \mathbf{0}, \tag{2.5}$$

where the elements of the structural mass and stiffness matrices are

$$M_{jk} = \rho_s h \int_A \Psi_j \Psi_k dA, \tag{2.6}$$

$$K_{jk} = \int_A [B]^T [\mathcal{D}][B] dA, \tag{2.7}$$

In Eq. (2.7), the $[B]$ and $[\mathcal{D}]$ matrices are given by

$$[B] = \begin{bmatrix} -\frac{\partial^2 \Psi}{\partial x^2} \\ -\frac{\partial^2 \Psi}{\partial y^2} \\ -2\frac{\partial^2 \Psi}{\partial x \partial y} \end{bmatrix}, \tag{2.8}$$

$$[\mathcal{D}] = \begin{bmatrix} 1 & \nu & 0 \\ \nu & 1 & 0 \\ 0 & 0 & (1-\nu)/2 \end{bmatrix}. \tag{2.9}$$

In the present study, the *in vacuo* structural mode shapes obtained from an FEA are used as the Ritz vectors in Eq. (2.1). The mode shapes are calculated using the commercial finite element package ANSYS. Fig. 2.1 shows a schematic of the plate model. The model mimics the physical configurations shown in Fig. 1.1 wherein the door is hinged at the top edge where it meets the fuselage and connected to a linear actuator on the interior surface. One of the plate edges parallel to the flow is hinged, allowing rotation about the x-axis while constraining all other degrees of freedom. A rectangular patch of nodes of width Δx and height Δy on the interior of the domain is pinned to model the ball joint of an actuator attachment. The location of the interior constraint is sampled at 2.5% intervals of chord and span across simulations. The domain is meshed using 1600 rectangular 4-node Kirchoff-Love plate elements. A convergence study was conducted on the highest-frequency structural configuration, and the 1600-element mesh yielded well-converged frequencies for the highest-order modes of interest. An example ANSYS code used for generating and solving the FEA model is shown in Appendix A.

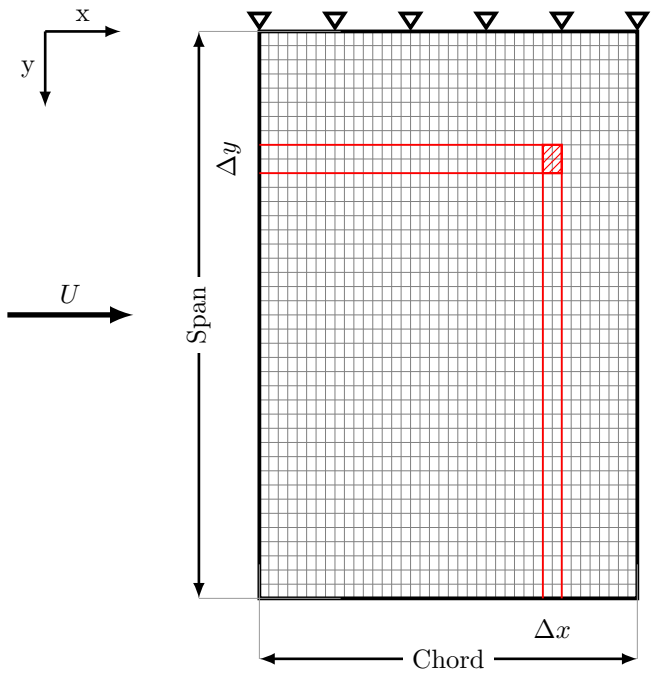

Figure 2.1. Geometry of the flat plate model. For all cases, a pinned boundary condition is applied to the edge at 0% span. This boundary condition fixes all degrees of freedom except for rotation about the x-axis. The hatched region indicates a representative rectangular patch of nodes where all translational degrees of freedom are fixed (with all rotational degrees of freedom left unconstrained).

In the VLM, the structural equations of motion must be discretized in time [43]. The equations are put into first-order form by letting $r_1 = q$ and $r_2 = \dot{q}$. The state variables are discretized at time step $n + \frac{1}{2}$ with step size Δt,

$$r_1^{n+\frac{1}{2}} = \frac{r_1^{n+1} + r_1^n}{2}, \tag{2.10a}$$

$$\dot{r}_1^{n+\frac{1}{2}} = \frac{r_1^{n+1} - r_1^n}{\Delta t}, \tag{2.10b}$$

$$r_2^{n+\frac{1}{2}} = \frac{r_2^{n+1} + r_2^n}{2}, \tag{2.10c}$$

$$\dot{r}_2^{n+\frac{1}{2}} = \frac{r_2^{n+1} - r_2^n}{\Delta t}. \tag{2.10d}$$

Substituting Eq. (2.10b) into Eq. (2.10c) yields a relationship between the state variables

$$\frac{r_1^{n+1} - r_1^n}{\Delta t} - \frac{r_2^{n+1} + r_2^n}{2} = 0. \tag{2.11}$$

Substituting Eqs. (2.10a) and (2.10d) into Eq. (2.5), the resulting discretized equation of motion is

$$[M]\left(\frac{\boldsymbol{r}_2^{n+1} - \boldsymbol{r}_2^n}{\Delta t}\right) + [K]\left(\frac{\boldsymbol{r}_1^{n+1} + \boldsymbol{r}_1^n}{2}\right) = \mathbf{0}. \tag{2.12}$$

Structural boundary conditions are specified during the creation of the *in vacuo* finite element model and are introduced to the structural model via the resulting mode shapes.

2.2 Fluid Model

For incompressible potential flow, the velocity potential, ϕ, is given by the Laplace equation [29]

$$\nabla^2 \phi = 0. \tag{2.13}$$

The Laplace equation is satisfied by a superposition of elementary solutions. Hence, a mesh of elementary solutions can be constructed to analyze a flow field. One such solution, the horseshoe vortex, is itself constructed of three vortex filaments. Two semi-infinite filaments parallel to the flow are connected at their endpoints by a third finite filament. All three filaments have equal circulation strength, Γ. The downwash velocity W_d at point g induced by a horseshoe vortex is derived from the Biot-Savart law [43],

$$W_d = -\frac{\Gamma}{4\pi}\int_c \frac{\boldsymbol{p}_g \times d\boldsymbol{s}}{\boldsymbol{p}_g^3}, \tag{2.14}$$

where $\boldsymbol{p}_g$ is the vector position of point g. In practice, it is convenient to define a kernel function that relates the strength of the horseshoe vortex circulation to the velocity field,

$$W_d = k(x, y)\Gamma(t). \tag{2.15}$$

The kernel function for a horseshoe vortex is given by Katz and Plotkin [35] as

$$k_{ij} = \frac{-1}{4\pi(y_i - y_{ja})}\left[1 + \frac{\sqrt{(x_i - x_{ja})^2 + (y_i - y_{ja})^2}}{x_i - x_{ja}}\right] + \frac{1}{4\pi(y_i - y_{jb})}\left[1 + \frac{\sqrt{(x_i - x_{ja})^2 + (y_i - y_{jb})^2}}{x_i - x_{ja}}\right], \tag{2.16}$$

where k is the influence coefficient due to the vortex geometry, x_a is the chordwise position of the finite-length vortex filament, and y_a and y_b are the spanwise positions of the lower and upper semi-infinite vortex filaments, respectively. A sample VLM mesh is shown in Fig. 2.2. The mesh consists of uniform rectangular elements of width δx and height δy. The mesh covers the structure and extends into the wake. Collocation points where continuity between the fluid and the structure is enforced are located at the three-quarter chord of each element. The horseshoe vortex is situated such that the finite filament lies at the quarter chord of the element and the semi-infinite filaments are coincident with the top and bottom of the element, as shown in Fig. 2.2. Assuming small structural deflections, the vortices are presumed to lie in the plane of the plate.

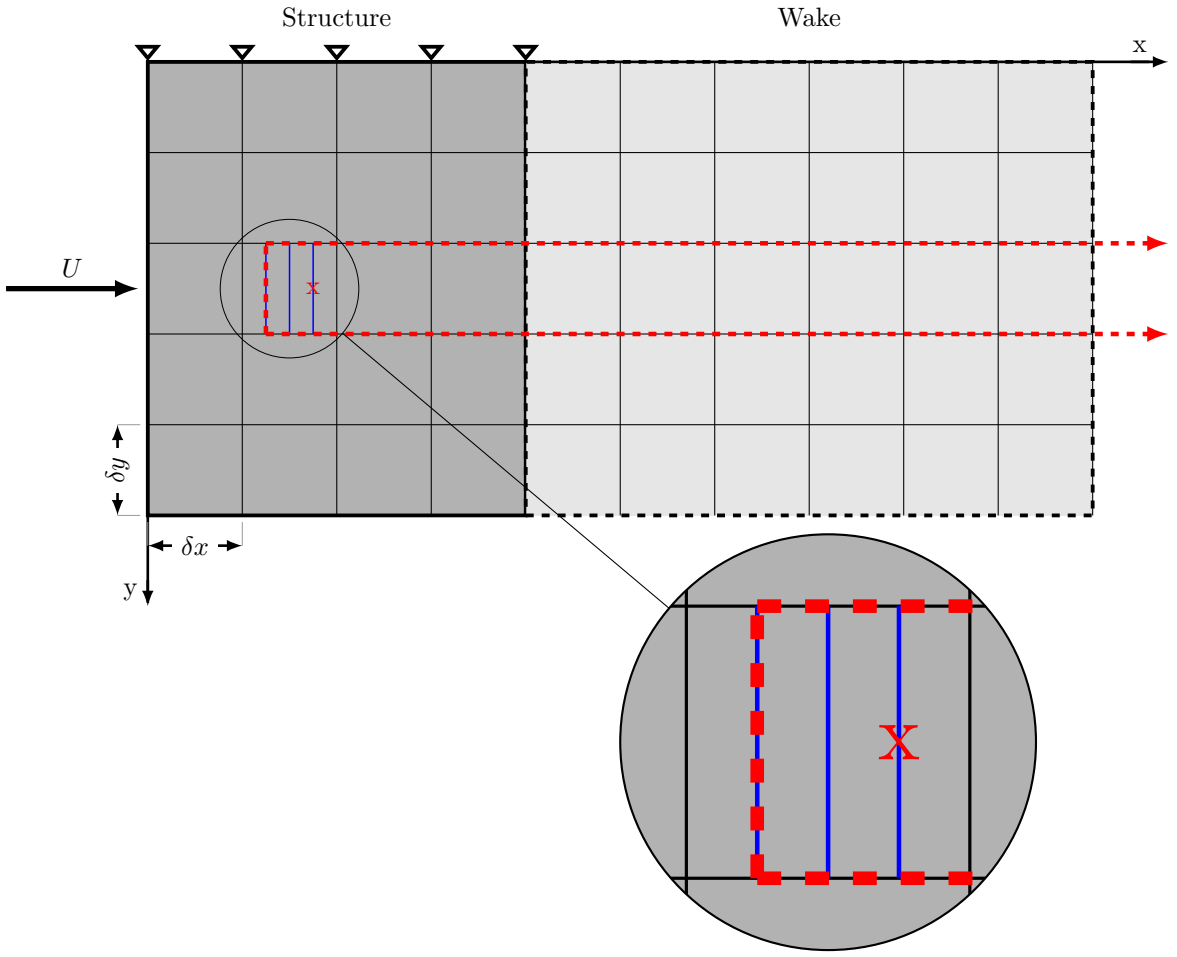

Figure 2.2. Sample fluid mesh. For each element there exists an associated horseshoe vortex as displayed on the second element of the third row. In the inset, the solid interior lines divide the example element into quarters and show that the finite-length vortex filament lies at quarter chord while the collocation point ("x") lies at three-quarter chord and mid span.

At each collocation point, the total downwash is equal to the structural velocity. The chain rule is applied to relate the velocity of the plate in fluid reference frame to the fixed reference frame associated with the plate,

$$W_d = \left(\frac{dw}{dt}\right)_{fluid} = \left(\frac{\partial w}{\partial t}\right)_{plate} + \frac{\partial x}{\partial t}\left(\frac{\partial w}{\partial x}\right)_{plate} = \left(\frac{\partial w}{\partial t}\right)_{plate} + U\left(\frac{\partial w}{\partial x}\right)_{plate}, \tag{2.17}$$

where U is the free-stream velocity. Substituting Eq. (2.1) into Eq. (2.17) and substituting the definitions of r_1 and r_2 into the result yields the downwash relationship in the form

$$[k]\mathbf{\Gamma}^{n+1} = [\beta]\boldsymbol{r}^{n+1} = \left[U\frac{\partial \Psi}{\partial x} \quad \Psi\right]\boldsymbol{r}^{n+1}, \tag{2.18}$$

where $[\beta]$ is the downwash matrix.

In the wake, the fluid behavior is prescribed by the vortices convected off the plate. At this point, it is useful to define the subscripts r and c to denote row, r, and column, c, of the rectangular fluid mesh. The vortex strength of each element in the first column of the wake, W_1 is related to the time rate of change of the upstream circulation strengths by

$$\Gamma^{n+1}_{r,W_1} = -\sum_{c=1}^{W_1-1}\left(\Gamma^{n+1}_{r,c} - \Gamma^{n}_{r,c}\right). \tag{2.19}$$

The second through the penultimate column of the wake are all defined by convection from the previous column. The circulation of these wake elements is given by

$$\Gamma^{n+1}_{r,c} = \Gamma^{n}_{r,c-1}. \tag{2.20}$$

The last column of the wake is similar to the other intermediate columns but includes a relaxation factor, α, to prevent the abrupt disappearance of the vortices at the end of the computational domain [61]

$$\Gamma^{n+1}_{r,c} = \Gamma^{n}_{r,c-1} + \alpha\Gamma^{n}_{r,c}. \tag{2.21}$$

In accordance with other studies [45, 50], the relaxation factor is set to 0.992.

The fluid also couples to the structure through a generalized force which is given by a sum over all the structural elements, n_s,

$$Q_m^{n+\frac{1}{2}} = \sum_{i=1}^{n_s}\Psi_{i,m}P_i^{n+\frac{1}{2}}, \tag{2.22}$$

Here, P_i represents the pressure on the i^{th} structural element and can be expressed through an application of the Bernoulli equation as a function of fluid density, ρ_f. and spanwise element length, δy,

$$P_{r,p}^{n+\frac{1}{2}} = \rho_f U \left(\frac{1}{2} \left(\Gamma_{r,p}^{n} + \Gamma_{r,p}^{n+1} \right) + \sum_{c=1}^{p} \left(\Gamma_{r,c}^{n+1} - \Gamma_{r,c}^{n} \right) \right) \delta y. \tag{2.23}$$

Substituting Eq. (2.23) into Eq. (2.22) yields an expression for the discrete generalized force in matrix form,

$$\boldsymbol{Q}^{n+\frac{1}{2}} = [C_1]\boldsymbol{\Gamma}^{n+1} + [C_2]\boldsymbol{\Gamma}^{n}. \tag{2.24}$$

2.3 Model Solution

The relevant equations from the previous two sections can be combined into a single equation of the form

$$\begin{bmatrix} [\sigma] & -[\beta] \\ -[C_1] & [D_1] \end{bmatrix} \begin{Bmatrix} \boldsymbol{\Gamma} \\ \boldsymbol{q} \end{Bmatrix}^{n+1} + \begin{bmatrix} [\xi] & [0] \\ -[C_2] & [D_2] \end{bmatrix} \begin{Bmatrix} \boldsymbol{\Gamma} \\ \boldsymbol{q} \end{Bmatrix}^{n} = 0, \tag{2.25}$$

where σ and ξ are the vortex influence terms from Eq. (2.16), β includes the downwash relationships from Eq. (2.18), C_1 and C_2 are the fluid forcing terms from Eq. (2.24), and D_1 and D_2 represent the structural equations of motion in Eq. (2.12). The model is solved by substituting assumed solutions of the form $\bar{\boldsymbol{\Theta}} e^{\lambda t}$ into Eq. (2.25), resulting in an eigenvalue problem of the form

$$\left(e^{\lambda \Delta t} \begin{bmatrix} [\sigma] & -[\beta] \\ -[C_1] & [D_1] \end{bmatrix} + \begin{bmatrix} [\xi] & [0] \\ -[C_2] & [D_2] \end{bmatrix} \right) \bar{\boldsymbol{\Theta}}_R = 0, \tag{2.26}$$

with discrete-time eigenvalues $\Lambda = e^{\lambda \Delta t}$ and system eigenvectors, $\bar{\boldsymbol{\Theta}}_R$. The continuous time eigenvalues λ are then calculated by

$$\lambda = \frac{\ln(\Lambda)}{\Delta t}. \tag{2.27}$$

The timestep is defined implicitly by forcing each vortex to convect downstream to the next downstream gridpoint over a distance of δx for every time Δt. Thus, the timestep is defined as

$$\Delta t = \frac{\delta x}{U}. \tag{2.28}$$

The viscous damping ratio, ζ, and temporal frequency, f, can be calculated directly from the eigenvalue using

$$f = \frac{\text{Im}(\lambda)}{2\pi}, \tag{2.29a}$$

and

$$\zeta = \frac{-\text{Re}(\lambda)}{\text{Im}(\lambda)}. \tag{2.29b}$$

The MATLAB implementation of the full aeroelastic VLM used in the present work is shown in Appendix B.

2.4 Eigenvalue Tracking

The eigenvalues calculated from Eq. (2.27) correspond to a single flow velocity. To investigate system stability, Eq. (2.26) is solved at several velocities both below and above the critical velocity. Most of the eigenvalues are associated with aerodynamic degrees of freedom, but the structural eigenvalues of primary interest typically have the largest real part and so are easily differentiated from the aerodynamic eigenvalues. It is important to find which structural mode corresponds to each eigenvalue to determine which mode goes unstable. However, the eigenvalues output from eigenproblem solvers are not in general sorted by mode, so an eigenvalue tracking routine must be implemented. At low flow speeds, the aeroelastic natural frequencies are similar to the *in vacuo* natural frequencies; thus, the first N imaginary parts of the eigenvalues ordered from smallest to largest correspond to the first N structural modes. Once all the structural modes have been initially linked to an eigenvalue, the eigenvalues are paired to the eigenvalues calculated in the next velocity step using the Hungarian assignment algorithm [62]. The pairing procedure is stepped across the the assumed values of free stream velocity to generate "eigenvalue tracks". The eigenvalue tracks are automatically generated and then visually checked for anomalies (e.g., abrupt changes). The resulting eigenvalue tracks allow the frequency and damping of each structural mode to be represented as a function of velocity.

The Hungarian algorithm was designed to solve the assignment problem. The details of the algorithm fall outside the scope of this thesis, but a detailed overview is given in Ref. [62], and an excellent MATLAB implementation is available in Ref. [63]. A version of the assignment problem may be roughly stated as, "If N workers take different amounts of time to complete each of M different jobs, how should the workers

be assigned to the jobs such that the total time spent working is minimized?" Furthermore, each worker may be assigned to no more than one job, and each job may have no more than one worker assigned to it. Mathematically, this problem may be described through the construction of a matrix $R_{N\times M}$ with elements corresponding to the "time" (cost) taken by the n^{th} worker to complete the m^{th} job. The goal becomes to find the smallest sum of elements such that exactly one element is taken from each row and each column. For the eigenvalue tracking problem, we wish to uniquely assign the set of structural modes to the set of eigenvalues at the next velocity step. The elements of the cost matrix are taken as the distances between each mode's eigenvalue at its current velocity and all potential eigenvalues at the next velocity. The Hungarian algorithm seeks to find pairings such that the total distance is minimized. Eigenvalues are tracked simultaneously, and no tracks are given priority. By formulating the problem this way, some of the challenges associated with naive nearest-neighbor techniques are overcome. In the author's experience, the Hungarian algorithm is able to capture eigenvalue crossing and veering phenomena better than nearest-neighbor trackers.

2.5 System Stability

Three different types of instability are of interest—divergence, flutter, and hump mode flutter. Divergence is characterized by a loss of structural stiffness, resulting in pure exponential growth of the solution. When the frequency associated with an eigenvalue track goes to zero, the corresponding mode has diverged. Flutter is characterized by unbounded growth of the harmonic response of a structural mode, and is identified when the damping of an eigenvalue track becomes negative. Negative damping corresponds to a positive real part of a system eigenvalue, which leads to exponential growth of the assumed solution. Hump mode flutter is similar, except the eigenvalue track returns to positive damping at a higher velocity. For the present study, a mode is said to be a hump mode if the damping becomes negative but later increases toward zero with increasing flow speed (resulting in an eigenvalue track resembling a "hump"). Hump modes often cause discontinuous jumps to small values of critical velocity across a parameter space, leading to difficulties in optimization procedures based on classical gradient-based techniques [64, 65]. These difficulties typically come about because the optimization procedure focuses on the lowest system critical velocity rather than the evolution of the eigenvalues. Methods based on eigenvalue separation constraints or mode tracking have been developed to avoid these difficulties [64]. For the present work, hump mode flutter may be of limited practical importance since the velocity at which a hump mode's damping again becomes positive is usually

higher than the critical velocity of another mode. In other words, even when the instability is hump mode flutter, the structure usually does not re-stabilize at higher flow speeds.

2.6 Fluid-Loaded Mode Extraction

The procedure for extracting the real-valued fluid-loaded structural mode shapes from the generally complex aeroelastic mode shapes is based on a complex modal analysis technique outlined in Ref. [66, 67]. The relevant equations are presented here without derivation. The left eigenvectors of Eq. (2.26) may be found through the solution of the adjoint eigenvalue problem,

$$\bar{\boldsymbol{\Theta}}_L^T \left(e^{\lambda \Delta t} \begin{bmatrix} [\sigma] & -[\beta] \\ -[C_1] & [D_1] \end{bmatrix} + \begin{bmatrix} [\xi] & [0] \\ -[C_2] & [D_2] \end{bmatrix} \right) = 0, \tag{2.30}$$

where $\bar{\boldsymbol{\Theta}}_L$ is the left eigenvector. The left and right eigenvectors have the same set of eigenvalues. Eqs. (2.26) and (2.30) each yield n pairs of eigenvalues and eigenvectors, each consisting of a unique complex vector and its complex conjugate. These may be rewritten in component form as,

$$\Lambda_j = \alpha_j + i\beta_j, \tag{2.31a}$$

$$\bar{\boldsymbol{\Theta}}_{Rj} = \boldsymbol{r}_j + i\boldsymbol{s}_j, \tag{2.31b}$$

$$\bar{\boldsymbol{\Theta}}_{Lj} = \boldsymbol{v}_j + i\boldsymbol{w}_j, \tag{2.31c}$$

A purely real basis may be formed from the complex eigenvalues and eigenvectors by neglecting the conjugate part of each eigenvalue and eigenvector pair, recognizing that the set of imaginary numbers is orthogonal to the set of real numbers, and applying a linear transformation to put the relevant equations in second-order form.

$$[\tilde{\Theta}_R] = [\boldsymbol{r}_1 - (\alpha_1/\beta_1)\boldsymbol{s}_1, (1/\beta_1)\boldsymbol{s}_1, ..., \boldsymbol{r}_n - (\alpha_n/\beta_n)\boldsymbol{s}_n, (1/\beta_n)\boldsymbol{s}_n], \tag{2.32a}$$

$$[\tilde{\Theta}_L] = [\boldsymbol{v}_1, \alpha_1\boldsymbol{v}_1 - \beta_1\boldsymbol{w}_1, ..., \boldsymbol{v}_n, \alpha_n\boldsymbol{v}_n - \beta_n\boldsymbol{w}_n], \tag{2.32b}$$

The aeroelastic coordinates may now be cast in terms of $[\tilde{\Theta}_R]$ and a new set of aeroelastic modal coordinates $\tilde{\xi}$, $\tilde{\eta}$,

$$\begin{Bmatrix} \boldsymbol{\Gamma} \\ \boldsymbol{q} \end{Bmatrix} = [\tilde{\Theta}_R] \left\{ \tilde{\xi}_1, \tilde{\eta}_1, \tilde{\xi}_2, \tilde{\eta}_2, ..., \tilde{\xi}_n, \tilde{\eta}_n \right\}^T. \tag{2.33}$$

Eliminating the rows of $[\tilde{\Theta}_R]$ associated with $\boldsymbol{\Gamma}$ and $\dot{\boldsymbol{q}}$ and eliminating the columns associated with $\tilde{\boldsymbol{\eta}}$ yields a relationship between the aeroelastic modal coordinates $\tilde{\boldsymbol{\xi}}$ and the structural modal coordinates $\boldsymbol{q}$

$$\boldsymbol{q} = [\tilde{\Theta}_q]\tilde{\boldsymbol{\xi}}, \tag{2.34}$$

where $[\tilde{\Theta}_q]$ is a mode shape matrix constructed by reducing the dimension of $[\tilde{\Theta}_R]$. Substituting Eq. (2.34) into Eq. (2.2) yields a relationship between displacement in physical coordinates and the aeroelastic modal coordinates

$$\boldsymbol{w} = [\psi][\tilde{\Theta}_q]\tilde{\boldsymbol{\xi}}(t), \tag{2.35}$$

The product $[\psi][\tilde{\Theta}_q]$ represents the displacement mode shape of the structure under the influence of aerodynamic loading. The MATLAB implementation of the complex modal analysis used in the present work is available in Appendix B.5.

2.7 Convergence

Convergence of the VLM depends on the number and arrangement of elements on the structure, the number of structural modes used, and the modeled length of the wake. Of these parameters, the configuration of mesh elements on the structure typically requires the most attention [45]. The structural mesh controls the resolution of the structural mode shapes. Hence, the use of higher-order modes with smaller wavelengths typically requires the use of more structural elements. Furthermore, Eq. (2.28) dictates that the timestep, and thus the highest resolvable frequency, is directly controlled by the free-stream velocity and the chordwise resolution of the structural mesh. Kohtanen [45] provides a detailed convergence study focused on the resolution of the mesh on the structure which confirms that convergence is improved at high flow speeds and low structural natural frequencies. Fig. 2.3 shows the first six structural frequencies for a plate with an aspect ratio (defined as the ratio of the plate's spanwise to chordwise lengths) of 0.33 in a flow speed of 1 m/s with a variety of structural mesh configurations. This plate represents the case with the highest natural frequency and lowest flow speed considered in the present work, so this figure represents a worst-case scenario. Both frequency and damping have converged to within 10% of the converged value for the first six modes with 200 chordwise elements and 30 spanwise elements, and to within 5% with 230 chordwise and 40 spanwise elements. Most cases are simulated using 50 chordwise and 60 spanwise elements; however, the cases

with $H = 1/3$ and $H = 2/3$ have significantly higher natural frequencies and are therefore run with 250 chordwise and 20 spanwise elements to ensure convergence at all simulation velocities by decreasing the timestep, as per Eq. (2.28). The number of elements in each direction was chosen to ensure convergence at velocities well below the critical velocity using VLM convergence results from Ref. [45].

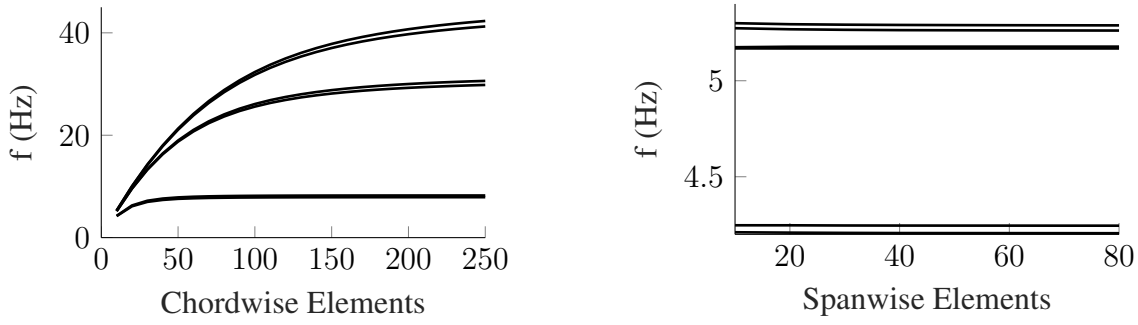

Figure 2.3. First six structural frequencies of a plate of aspect ratio 0.33 in a flow speed of 1 m/s using (a) a number of chordwise elements and 10 spanwise elements, and (b) a number of spanwise elements and 10 chordwise elements.

As more structural modes are included in the analysis, convergence is quickly achieved. Fig. 2.4 plots the first and second calculated frequency of the same plate shown in Fig. 2.3 for an increasing number of included structural modes. Both frequencies and the corresponding damping values have converged once three modes are included in the analysis. However, six modes are used in the present work to accurately capture the effects of fluid loading on the first five modes. Since it is typically necessary to include modes in the analysis beyond the highest mode of interest, results for the sixth mode cannot be trusted.

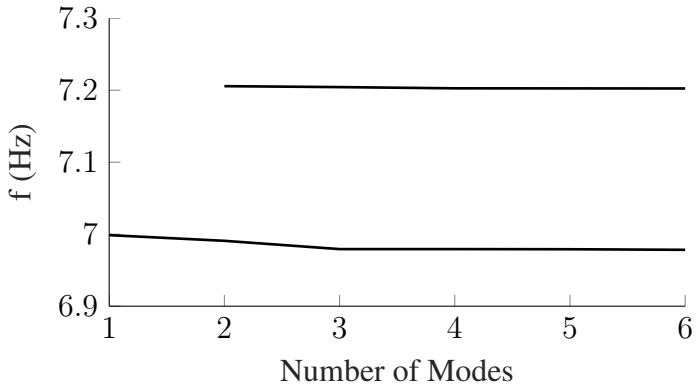

Figure 2.4. First two frequencies of a 0.33 aspect ratio plate as a function of the number of included modes.

Accurate modeling of the aerodynamics requires a sufficiently long wake region. Fig. 2.5 shows wake length versus the first six frequencies for a plate with an aspect ratio of 2.67. Previous work has shown that the effects of the wake diminish as the plate dimension perpendicular to the stream decreases relative to the streamwise dimension [68]. Fig. 2.5 represents a worst-case convergence scenario since all aspect ratios used in the present work are less than or equal to 2.67. Both frequency and damping have converged to within 10% of the converged value for all modes with a wake-to-chord ratio of less than 0.5 and to within 5% with a wake-to-chord ratio of 1. A wake-to-chord ratio of 0.5 is used for all cases presented here.

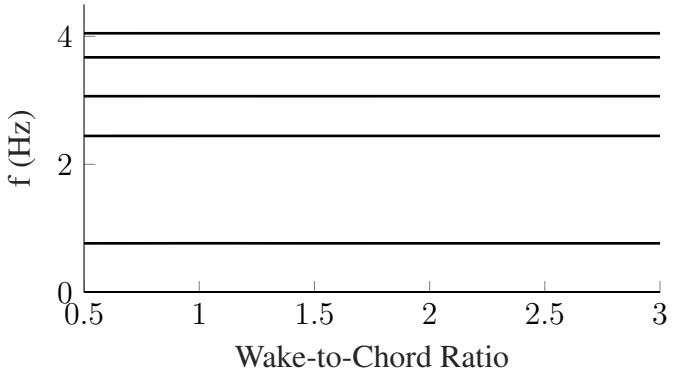

Figure 2.5. First six frequencies of a 2.67 aspect ratio plate with various wake lengths.

Chapter 3

Numerical Studies

3.1 Simulation Setup and Parameter Study Map

The aspect ratio of the plate, H, mass ratio, μ, and footprint size of the actuator, A_f, are varied across simulations. The aspect ratio is defined as the ratio of the plate's spanwise to chordwise lengths, $H = a/b$, and is changed by varying the span length while keeping the chord length constant. The mass ratio is defined as $\mu = 4\rho_s h/(\pi\rho_f b)$, and is changed by varying the density of the fluid. The properties for a nominal case are shown in Table 3.1. The material properties are consistent with aluminum, a common material for aerospace applications. The fluid density is nominally consistent with air, but for the cases in which mass ratio is varied, fluid density is changed to achieve the desired mass ratio. It is noted that the plate thickness of 1 mm is considerably thinner than is realistic for typical landing gear doors. This value was chosen to reduce the computational expense of the parameter study. Due to their lower natural frequencies, thin plates require fewer chordwise elements to converge than do thick plates, as per Eq. (2.28). A preliminary study by the authors [69] considered an 8 mm-thick plate and showed that the sensitivity of instability mode to postulated actuator placement is very similar to what is reported here. Thus, we expect the critical instability mode and the reduced critical velocities to be insensitive to plate thickness.

The parameters are varied one at a time starting with this nominal case. There are no cases in which two parameters are varied simultaneously, and the parameter values for the different cases are given in Fig. 3.1. Besides the nominal case, there are three cases varying aspect ratio, four cases varying mass ratio, and three cases varying pinned footprint area, for a total of eleven configurations.

For each of the 11 configurations, a total of 1521 (39 spanwise by 39 chordwise) postulated actuator locations are considered. This results in 16731 simulation cases, each involving the solution of the eigen-

problem for at upwards of 40 discrete flow velocities. Simulations were run in several batches of parallel jobs using the Georgia Advanced Computing Resources Center (GACRC). A total of approximately 1,000,000 core-hours were used to complete the simulations.

Table 3.1. Material properties and geometry of the nominal case.

Property	Symbol	Value
Span	a	1.5 m
Chord	b	0.9 m
Aspect Ratio	H	1.67
Thickness	h	1 mm
Footprint Size Ratio	A_f/A	0.25 %
Young's Modulus	E	70 GPa
Poisson's Ratio	ν	0.3
Structural Density	ρ_s	2700 kg/m^3
Fluid Density	ρ_f	1.23 kg/m^3
Mass Ratio	μ	3.105

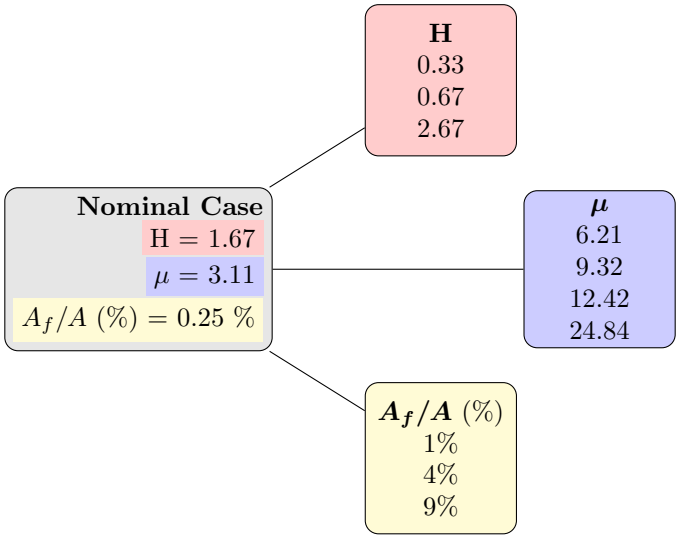

Figure 3.1. Map of the parameter study. Starting with the nominal case, each parameter is varied independently across the values in the associated branch.

3.2 In Vacuo Structural Results

3.2.1 Natural Frequencies

It is useful to understand how the placement of the actuator changes the natural frequencies of the *in vacuo* structure since the critical flutter and divergence velocities are expected to be proportional to natural frequency [4, 17, 18]. Fig. 3.2 shows normalized natural frequencies for the first six modes of the plate as a function of postulated actuator placement. For each mode, the natural frequencies are normalized by the largest natural frequency found for each mode (2.76, 2.83, 4.83, 6.51, 8.90, and 9.65 Hz). For all modes, but especially the first two, the natural frequency increases as the spanwise location of the actuator increases. While the natural frequencies of all modes are affected by the placement of the interior boundary condition, the low-order modes are affected much more than the higher-order modes. The lowest natural frequency of the first mode is approximately 10% of the highest value, while the lowest natural frequency of the sixth mode is approximately 80% of the maximum.

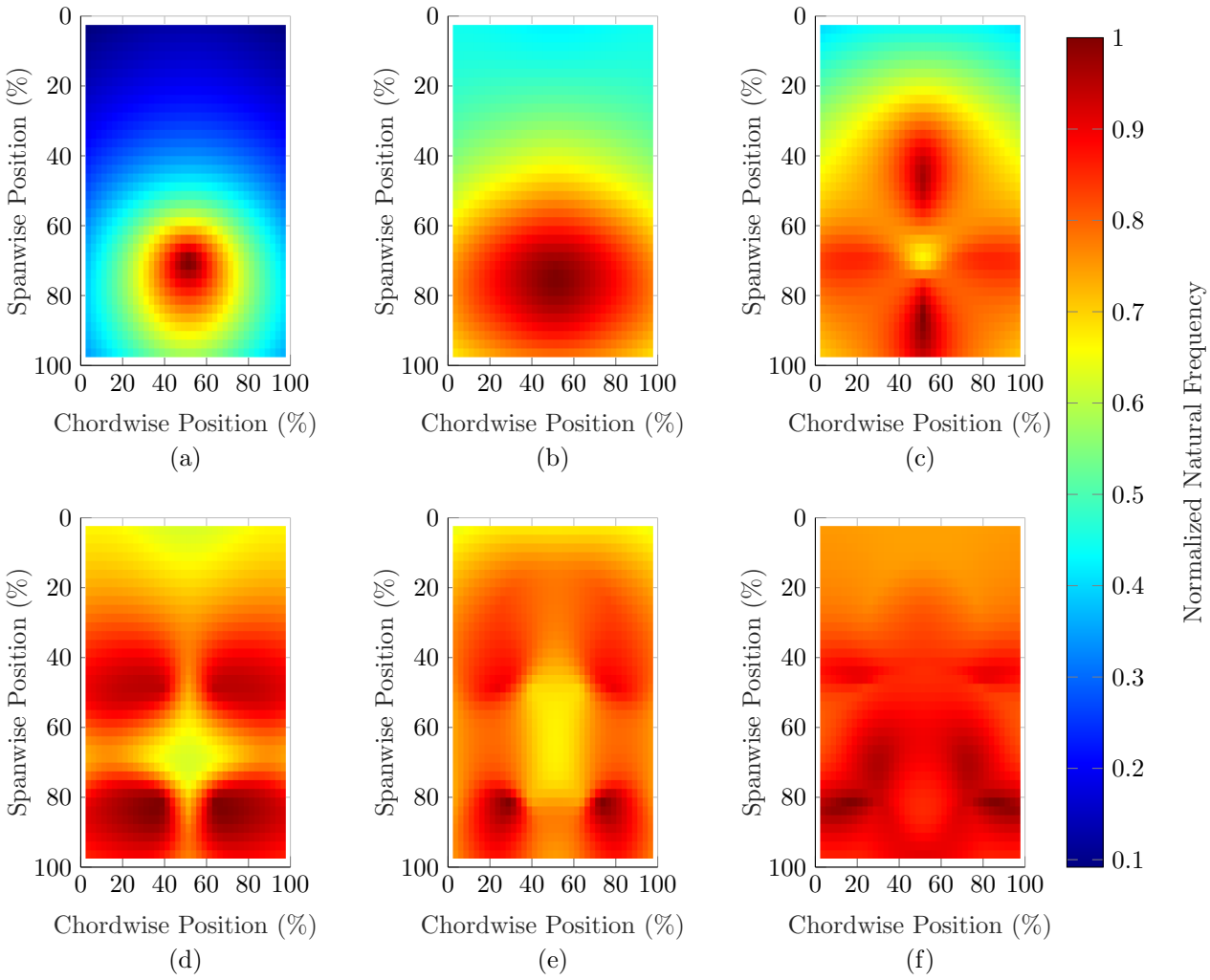

Figure 3.2. (a) First, (b) second, (c) third, (d) fourth, (e) fifth, and (f) sixth natural frequencies of the plate as a function of actuator position. The natural frequencies are normalized by the greatest natural frequency found for each mode.

3.2.2 *In Vacuo* Mode Shapes

Sample *in vacuo* mode shapes are shown in Fig. 3.3 for the case in which the simulated actuator is placed at 50% of span and 50% of chord. Because of the cluster of pinned nodes simulating the actuator, the mode shapes do not always resemble those of a classical flat plate. For instance, while the shape of the first mode is similar to that of a typical (1,1) cantilevered plate mode and the second mode is similar to a (1,2) mode, the third through sixth modes are more difficult to classify and describe. Additionally, the mode shapes are significantly affected by the location of the pinned interior nodes, and the mode shapes shown in Fig. 3.3 correspond to just a single case.

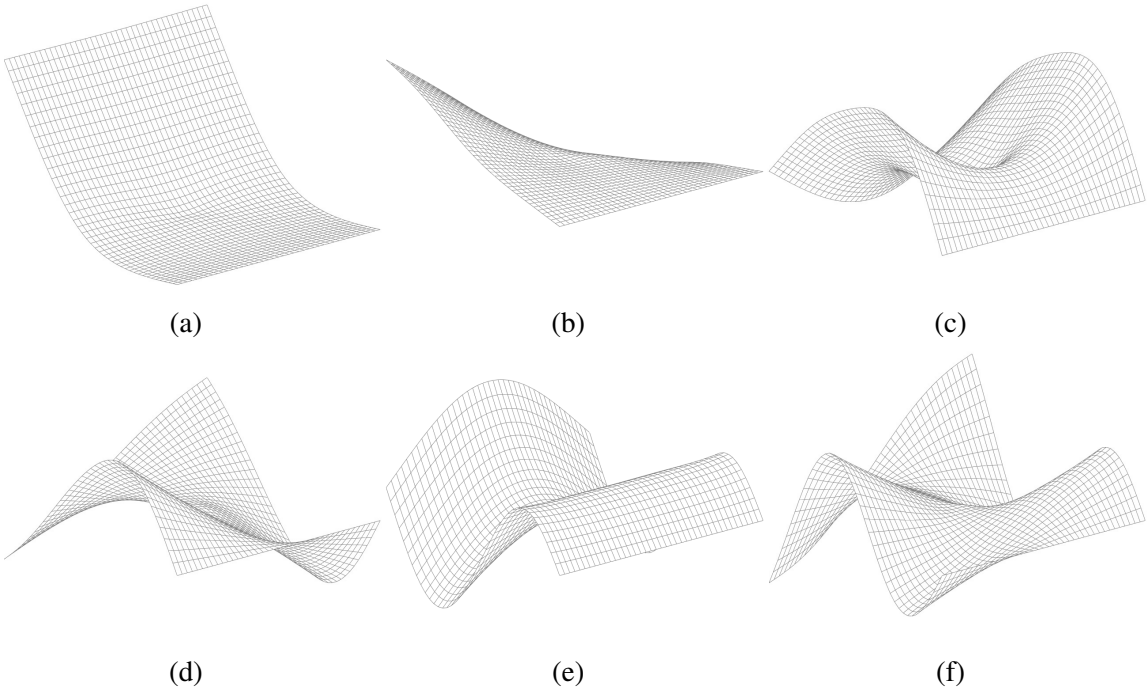

Figure 3.3. (a) First, (b) second, (c) third, (d) fourth, (e) fifth, and (f) sixth mode shapes for an arbitrarily chosen 50% chordwise, 50% spanwise pinned boundary condition.

To observe how the postulated location of the actuator affects the *in vacuo* mode shapes, Fig. 3.4 shows the first mode shape of the plate for three different locations of the pinned internal boundary condition (50% chord, 2.5% span, 50% chord, 97.5% span, and 97.5% chord, 50% span). In the first case, the first mode looks like a classical (1,1) cantilevered plate mode. Moving the internal boundary condition down the span (as in the second case) results in a first mode shape that resembles the first mode of a pinned-free-pinned-free plate. When the internal boundary condition is moved off the mid-line in the third case, the first mode shape most closely resembles the (1,2) chordwise bending mode of a cantilevered plate. The sensitivity of the mode shapes to the internal boundary conditions foreshadows a similar sensitivity of the aeroelastic results.

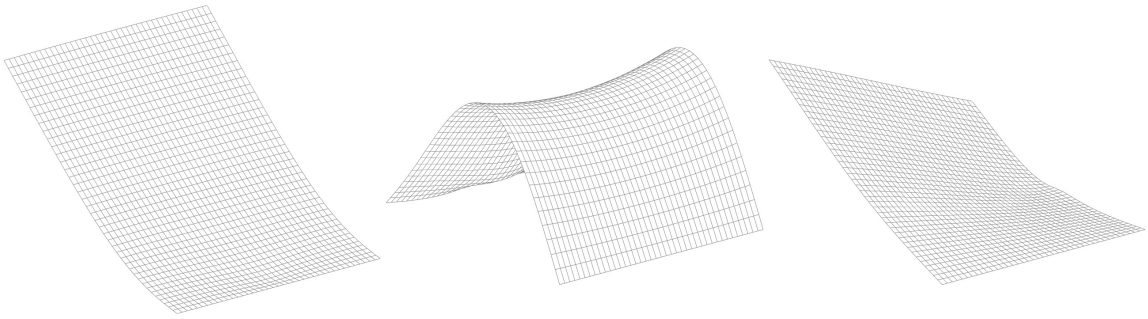

(a) (b) (c)

Figure 3.4. First structural mode of the nominal case with the internal boundary condition positioned at (a) 50% chord, 2.5% span, (b) 50% chord, 97.5% span and (c) 97.5% chord, 50% span.

3.3 Aeroelastic Results

3.3.1 Typical Aeroelastic Behavior

Before discussing how the aeroelastic instability of the plate changes with aspect ratio, mass ratio, and actuator footprint size, the typical behavior with respect to postulated actuator placement is considered. We define normalized damping, $\hat{\zeta}$,

$$\hat{\zeta} = \frac{-\text{Re}(\lambda)}{\sqrt{\text{Re}(\lambda)^2 + \text{Im}(\lambda)^2}} = \frac{-\text{Re}(\lambda)}{|\lambda|}, \tag{3.1}$$

Normalizing damping in this way bounds $\hat{\zeta}$ between ∓ 1 and simplifies the identification of instabilities. Fig. 3.5 shows $\hat{\zeta}$ for the first four eigenvalues of the nominal plate with the interior boundary conditions placed at 30% span and 5%, 50%, and 95% of chord. The system is stable for positive values of normalized damping and unstable for negative values. When $|\hat{\zeta}| = 1$, the corresponding mode's natural frequency has gone to zero, indicating divergence. Note that moving the boundary condition along the chord changes the type of instability. When the boundary condition is at 5% of chord the critical instability is second mode flutter. At 50% of chord, hump mode flutter of the second mode is critical, and when the boundary condition is at 95% of chord, the plate goes unstable by divergence.

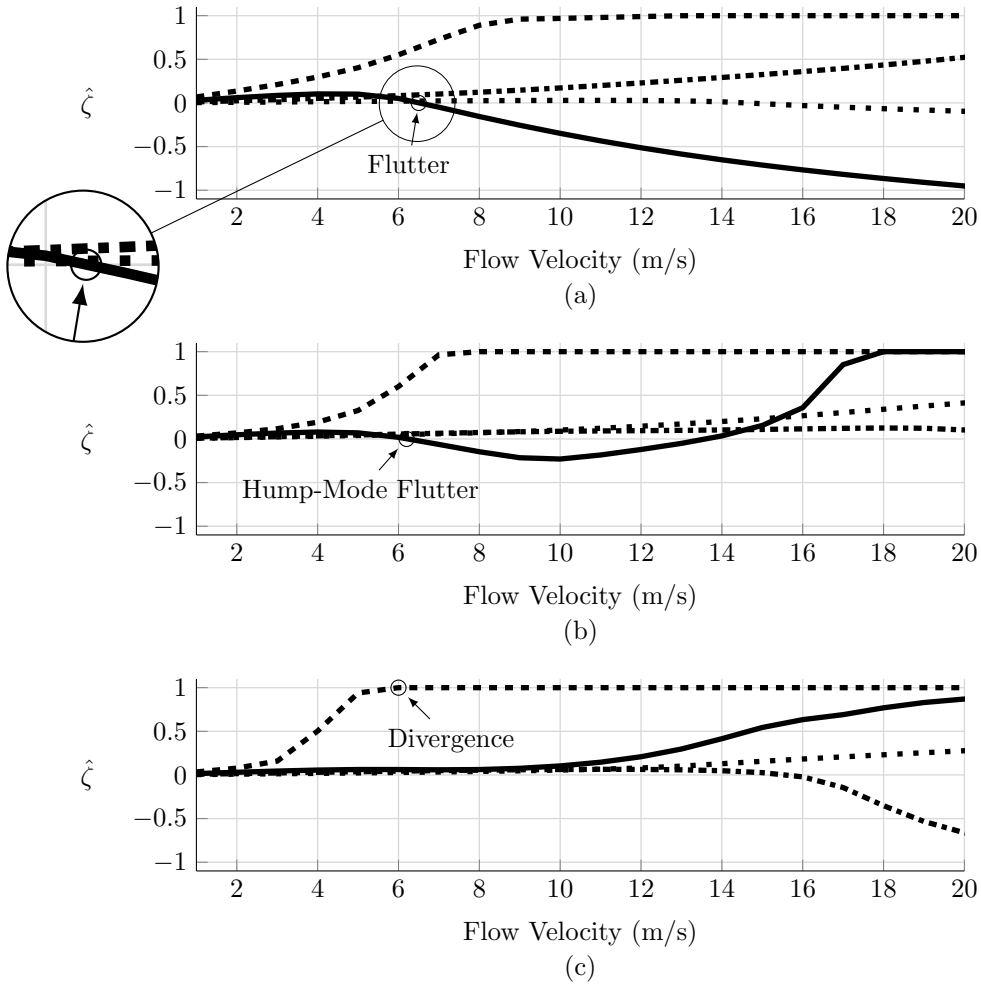

Figure 3.5. Normalized damping of the first (dashed), second (solid), third (dash-dotted), and fourth (dotted) modes for the nominal plate with the actuator positioned at 30% span and (a) 5%, (b) 50%, and (c) 95% chord.

Fig. 3.6 maps the type of instability and the corresponding mode number across the full range of postulated actuator placements for the nominal plate described in Table 3.1. The features of this map are typical of the plate configurations studied here. Second-mode flutter dominates at low chord placements, whereas divergence dominates at high chord placements. In general, the location of the boundary between flutter and divergence changes with the spanwise location of the postulated actuator. As the actuator is positioned closer to the trailing edge, the flutter velocity typically increases while the divergence velocity simultaneously decreases. The boundary between the flutter and divergence regions occurs when the divergence velocity drops below the flutter velocity, similar to the results seen in Ref. [20]. There is also a small region at high span and low chord at which the critical instability is associated with higher-order modes.

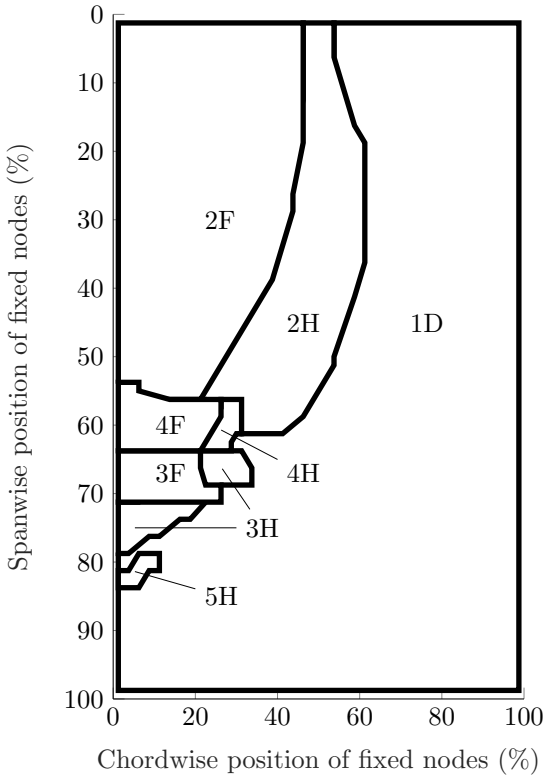

Figure 3.6. First unstable structural mode (denoted by the number) and the type of instability (D - divergence, F - flutter, H - hump) for various postulated actuator positions on the nominal plate configuration.

The critical flow velocity, U_{cr}, of the nominal plate configuration is shown in Fig. 3.7(a) for all postulated actuator positions. Note that the low critical velocities reported here are due to the small thickness chosen for each plate. In general, the critical velocities increase when the actuator is postulated at higher percentages of the span. This is related to the fact that *in vacuo* natural frequencies tend to increase when the actuator is postulated at higher percentages of span (see Fig. 3.2). When the actuator is placed at a high chordwise location, the critical velocity changes quickly as the postulated placement crosses the flutter-divergence boundary. Fig. 3.7(a) indicates that actuator placement can have nearly a fourfold effect on critical velocity.

In Fig. 3.7(b), the flutter frequency is shown across the range of postulated actuator positions where flutter is predicted. The frequencies are normalized by the corresponding *in vacuo* natural frequency for a given placement of the actuator. This isolates the effects of fluid interaction. The flutter frequency tends to be more similar to the natural frequency at high span, with low-span locations having normalized flutter frequencies much less than unity.

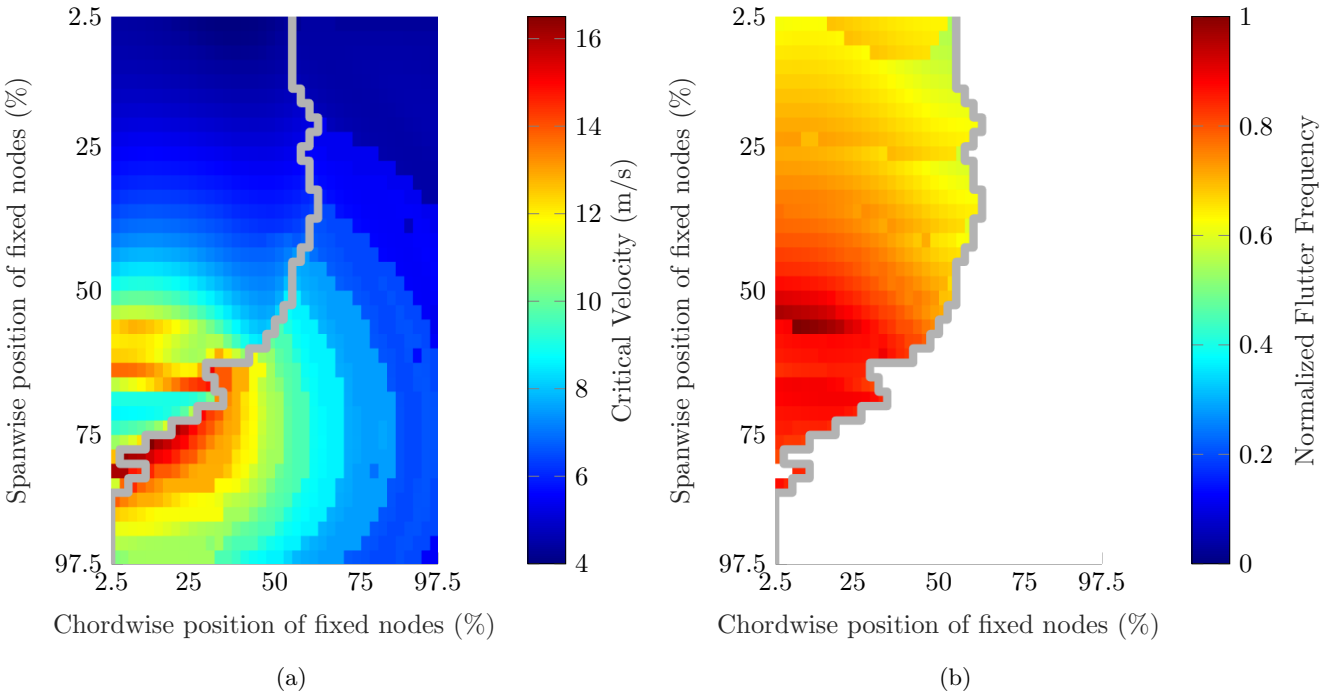

Figure 3.7. (a) Critical velocity and (b) flutter frequency as a function of actuator position. For a given actuator placement, the frequencies in (b) are normalized by the *in vacuo* natural frequency of the fluttering mode. The gray line overlays show the boundary between flutter (left) and divergence (right).

3.3.2 Parameter Study

The effects of different parameters on system instability are now discussed. The flutter-divergence boundaries for the cases varying spanwise length, fluid density, and actuator footprint size are shown in Fig. 3.8. Aspect ratio has the greatest influence on the shape of the boundary, followed by mass ratio. The size of the actuator footprint has little effect on the shape of the boundary. As the aspect ratio increases, the boundary moves toward the trailing edge near the root and toward the leading edge near the tip. At high aspect ratios, the boundary curves from mid-chord at very low span, to high chord, and then back to mid-chord at around mid-span. The boundaries for all the cases with different aspect ratios intersect when the actuator placement is at approximately 20% chord and 70% span. As the mass ratio increases, the boundary moves closer to the trailing edge at high spanwise locations. The boundary appears to remain nearly stationary once the mass ratio is greater than about ten.

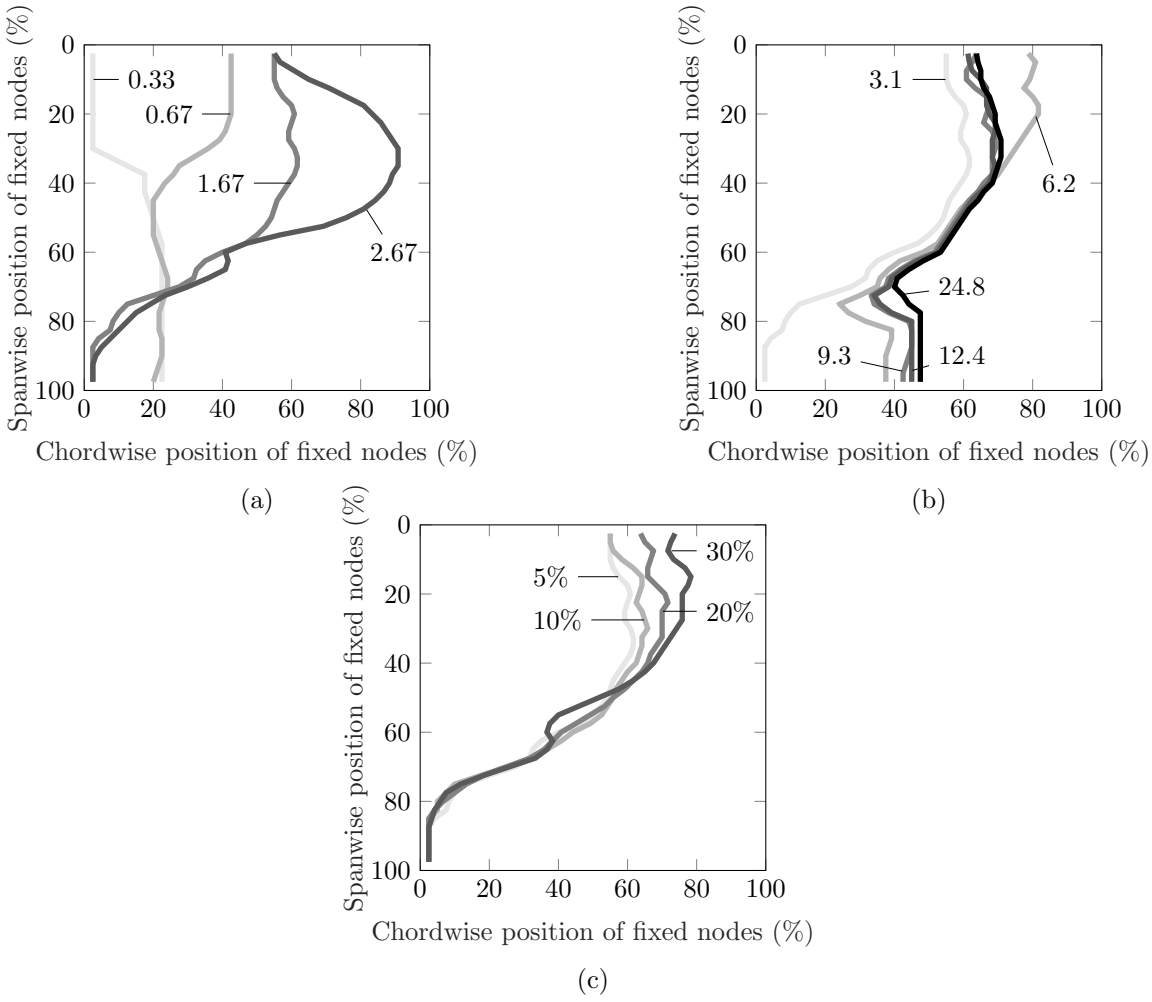

Figure 3.8. Flutter-divergence boundary shape and location as a function of (a) aspect ratio, (b) mass ratio, and (c) footprint size. For all cases, flutter occurs when the actuator is positioned to the left (upstream) of the boundary while divergence occurs for actuator positions to the right (downstream) of the boundary.

Two important design parameters are the value of the largest critical velocity that may be achieved, and the location of the actuator needed to achieve this velocity. The markers in Fig. 3.9 shows the actuator placement that maximizes critical velocity for all of the configurations considered in the parameter study. The markers indicate the parameter being varied, and the arrows indicate the direction of the parameter's increase. The color of the markers in Fig. 3.9a represents the critical velocity while the corresponding reduced critical velocities ($U^*_{cr} = U_{cr}/bf$, where f is the *in vacuo* natural frequency of the critical mode expressed in Hz) are shown in Fig. 3.9b. The actuator location where the largest critical velocity occurs changes little with aspect ratio or mass ratio, staying near 80% span and 20% chord. As the footprint size

increases, the location of the largest critical velocity moves from approximately 10% chord and 75% span to 40% chord and 60% span.

By normalizing by natural frequency, the reduced critical velocities shown in Fig. 3.9b isolate the aeroelastic effects of changing different parameters. As aspect ratio increases, the largest critical reduced velocity tends to decrease. This decrease may be caused by larger aerodynamic moments about the hinge and actuator. As mass ratio increases, the largest reduced critical velocity increases nearly linearly. This is expected since Eq. (2.23) indicates that the dynamic pressure on the structure is inversely proportional to the mass ratio. As the fixed-node footprint area increases, the dimensional critical velocity decreases, as seen in Fig. 3.9a. Increasing the footprint of the internal boundary condition stiffens the structure leading to larger natural frequencies and higher critical velocities. However, removing the effects of these natural frequency changes by expressing the results in terms of reduced critical velocity (Fig. 3.9b) reveals that a larger fixed-node footprint actually destabilizes the structure from an aeroelasticity perspective.

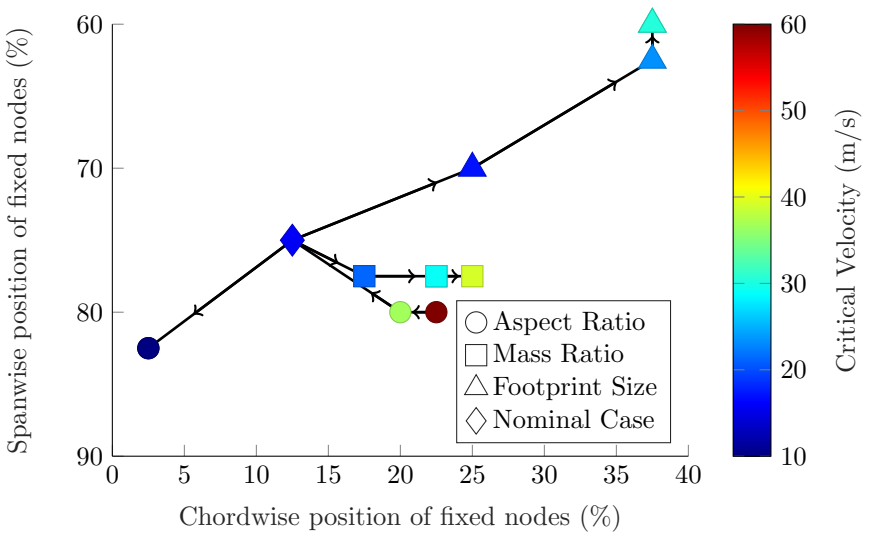

(a)

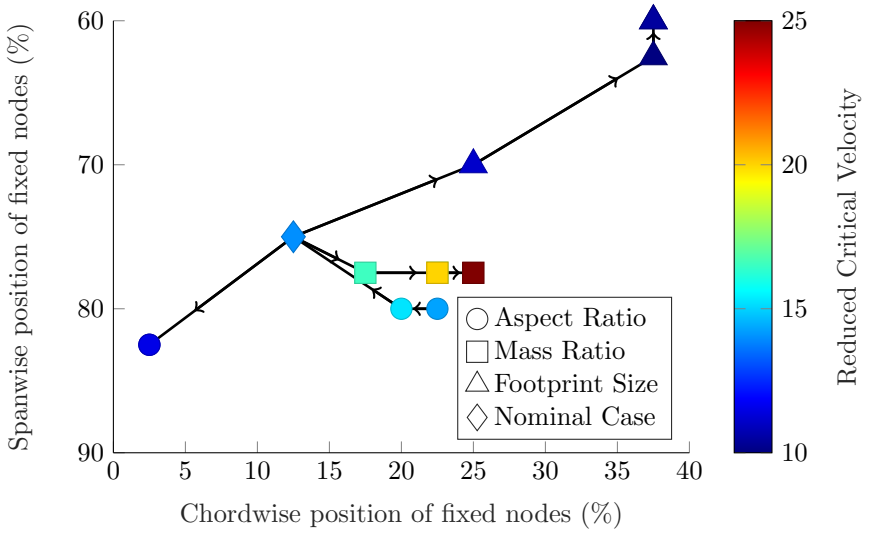

(b)

Figure 3.9. Location of the cluster of fixed nodes at which the largest critical velocity is achieved for varying aspect ratio (circles), mass ratio (squares), and footprint size (triangles). All parameter studies intersect at the nominal case (diamond). The (a) critical velocity, and the (b) corresponding reduced critical velocity are shown as the marker color.

3.4 Discussion of Key Results

3.4.1 High-Order Instability

We first attempt to explain the high-order mode flutter that is predicted when the actuator is positioned at relatively low chord and high span locations (see Fig. 3.6). To do this, we use the modal assurance criterion (MAC), an indicator of the spatial similarity between two mode shapes. The MAC is defined as

$$\text{MAC}_{ij} = \frac{|\hat{\phi}_i^T \hat{\phi}_j|^2}{(\hat{\phi}_i^T \hat{\phi}_i)(\hat{\phi}_j^T \hat{\phi}_j)}, \tag{3.2}$$

where $\hat{\phi}$ is a mode shape and i and j are indices. The baseline mode is defined as the second (i.e., critical) mode of the nominal plate with the actuator placed at 50% chord and 50% span. The MAC is then calculated by comparing the baseline mode to each of the first six modes of the same plate for the range of postulated actuator placements. For each case, the mode with the largest MAC value is identified as being the most spatially similar to the baseline. The results of this analysis are shown in Fig. 3.10. The results show that the baseline mode (which is a second mode) is most similar to the first or third modes when the actuator is positioned at mid-to-high span and near the leading or trailing edge. In Fig. 3.6, it was observed that higher-order mode flutter occurs when the actuator is positioned at mid-to-high span and near the leading edge. Thus, we believe that these regions of higher-order mode flutter can be at least partially explained by recognizing that actuator placements at mid-to-high span and near the leading edge result in higher-order modes that are spatially similar to the nominal second mode of the plate.

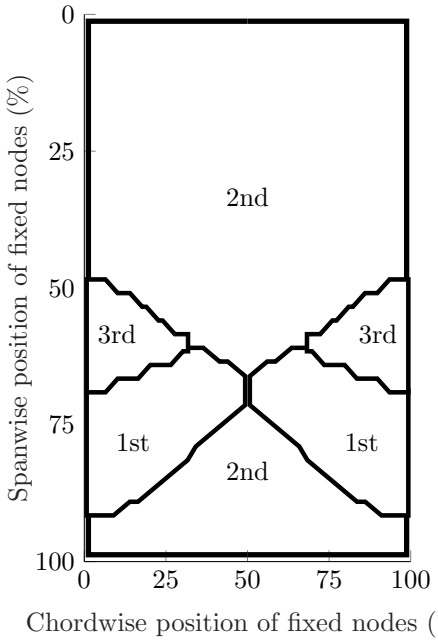

Figure 3.10. Mode at each actuator position with the most similarity to a nominal mode as determined by the MAC value. The nominal mode is taken as the second structural mode when the actuator position is prescribed at mid chord and span.

The mode shapes observed in flow may differ from the *in vacuo* modes. For the following discussion, we refer to the structural modes obtained from FEA as *in vacuo* or *structural* modes, and the modes obtained using the complex modal analysis method discussed in Ch. 2.6 as *aeroelastic* or *fluid-loaded* modes. The *in vacuo* modes may couple together in a fluid flow, resulting in aeroelastic modes that are a combination of the two coupled modes. Modal coupling is often accompanied by a frequency veering phenomenon, wherein the system frequencies associated with the two coupling modes first approach each other and then veer away as a parameter (in this case flow velocity) increases. Fig. 3.11 shows the frequency of the first two eigenvalues of the nominal case with the actuator positioned at 2.5% span and 47.5% chord. At low velocity, the second mode decreases in frequency, approaching the frequency of the first mode. Near the critical velocity, the two frequency tracks veer away from each other with the second frequency slightly curving upward and the first frequency curving toward zero. Since the veering phenomenon occurs very near the flutter velocity, we expect the first two modes to experience coupling.

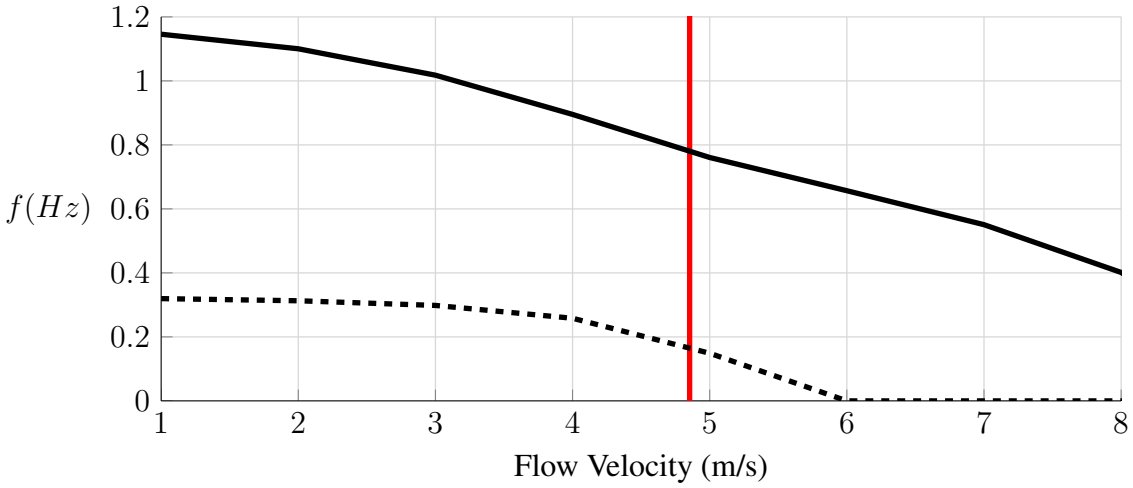

Figure 3.11. Frequency of the first (dashed) and second (solid) modes for the nominal plate with the actuator positioned at 2.5% span and 47.5% chord. The vertical red line indicates the critical velocity at 4.85 m/s.

Coupled aeroelastic modes may be described in terms of the input structural modes. The MAC is again used to inform this discussion. For a postulated actuator position and corresponding critical velocity, Eq. (3.2) is used to compare the spatial similarity between the unstable aeroelastic mode i and the first six structural modes. If a MAC value between fluid-loaded mode i and structural mode j is greater than an arbitrarily chosen value of 30% of the MAC value between aeroelastic mode i and structural mode i (i.e., $MAC_{ij} > 0.3MAC_{ii}$), significant modal coupling has occurred between modes i and j. Fig. 3.12 shows postulated actuator positions where modal coupling occurs at the first critical velocity for the nominal case and the parameter study case with $\mu = 24.84$. The marker colors indicate the unstable aeroelastic mode associated with the first critical velocity (similar to Fig. 3.6) and the marker shape indicates the coupling structural mode. The region where first-mode divergence dominates is not checked for coupling because divergence is characterized by a sudden loss of stiffness, so the concept of modal coupling at divergence is not applicable.

For the nominal case, all configurations where second-mode flutter dominates exhibit coupling with the first structural mode, and the aeroelastic mode shape is much more similar to the first than the second structural mode. Fig. 3.13a shows an example MAC diagram for the nominal case indicating the influence of each structural mode on each aeroelastic mode. The coupling of the first two modes results in flutter mode shapes which contain a first mode (bending) component in addition to the second mode (torsion) component,

similar to classical bending-torsion flutter. In the high-span, low-chord region, coupling is also present. The critical aeroelastic modes in the regions of third and fourth mode flutter exhibit spatial similarity with low-order structural modes. At the boundary between the third- and fourth-mode flutter regions, the third structural mode is spatially similar to the fourth aeroelastic mode (green triangular markers), suggesting a smooth transition of the aeroelastic mode shapes as this boundary is crossed.

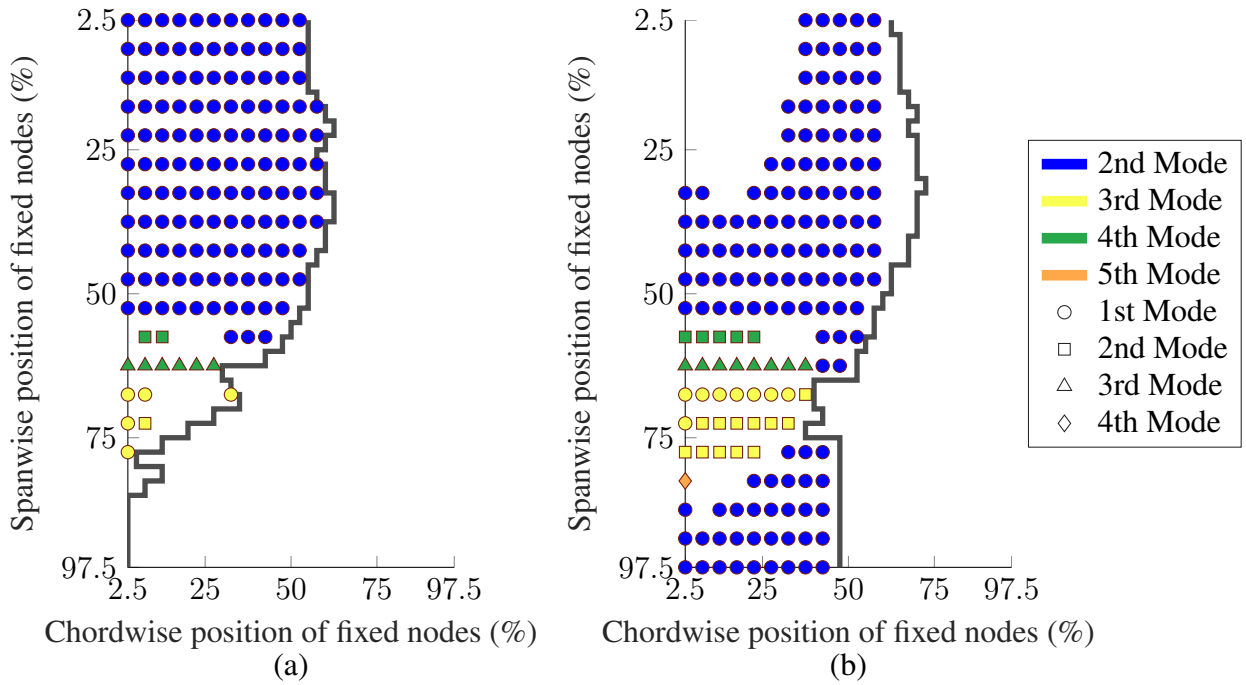

Figure 3.12. First unstable aeroelastic mode (marker color) and the coupling in vacuo mode (marker shape) for (a) the nominal case and (b) the case with $\mu = 24.84$. The gray line overlays show the boundary between flutter (left) and divergence (right). Only postulated actuator positions that demonstrate coupling are shown. The region near the boundary in (b) that does not show modal coupling is actually inconclusive.

The results for the high-order mode flutter regions observed for the nominal case hold for the high mass ratio case, with the high-order aeroelastic modes sharing spatial similarity with low-order structural modes. As in the nominal case, the third and fourth aeroelastic modes again display significant contributions from the fourth and third *in vacuo* modes, respectively. However, many of the aeroelastic mode shapes observed in the second mode flutter region do not exhibit significant contributions from *in vacuo* modes other than the second. That is, there are regions of parameter space in which the flutter modes are not appreciably coupled and the system exhibits single-mode flutter. Note that in Fig. 3.12b the region near the flutter-divergence boundary that appears to experience single-mode flutter is actually inconclusive. Most likely this region

experiences modal coupling between the first two modes, but an unresolved computational error prevents the calculation of these system mode shapes. Fig. 3.13b shows an example MAC diagram for the $\mu = 24.84$ case.

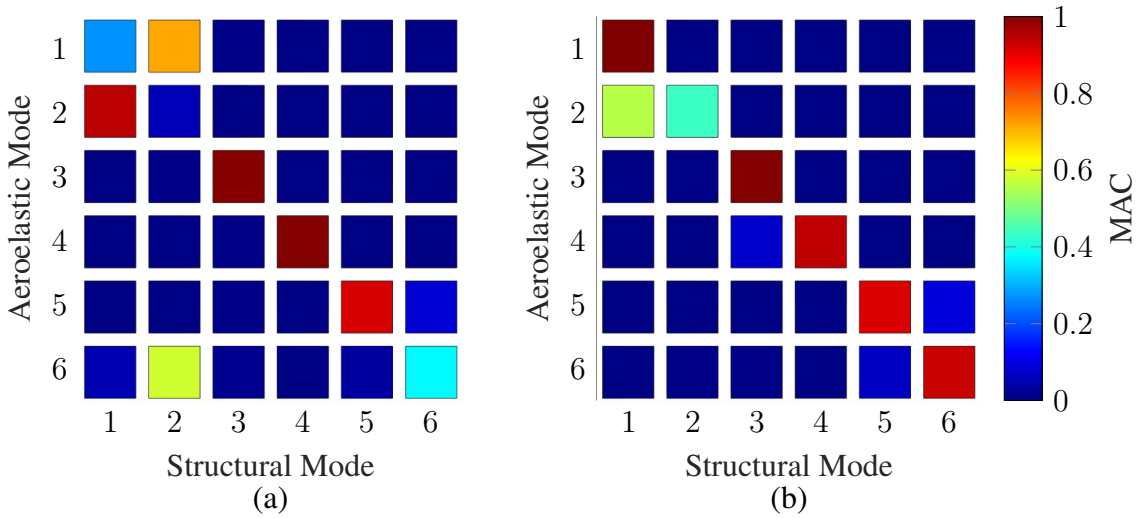

Figure 3.13. MAC plots showing the similarity between each aeroelastic mode (rows) and each *in vacuo* mode (columns) for (a) the nominal case, and (b) the $\mu = 24.84$ case for a postulated actuator positioned at 47.5% chord, 2.5% span.

Fig. 3.14 shows a comparison of the second aeroelastic mode shape for the two different cases. The postulated actuator position at 47.5% chord, 2.5% span yields coupled-mode flutter in both cases. Note that the flutter mode from the nominal case is similar to a first-order bending mode ($MAC_{21}/MAC_{22} = 18.3738$) while the flutter mode from the $\mu = 24.84$ case is more similar to a first-order torsion mode ($MAC_{21}/MAC22 = 1.28$).

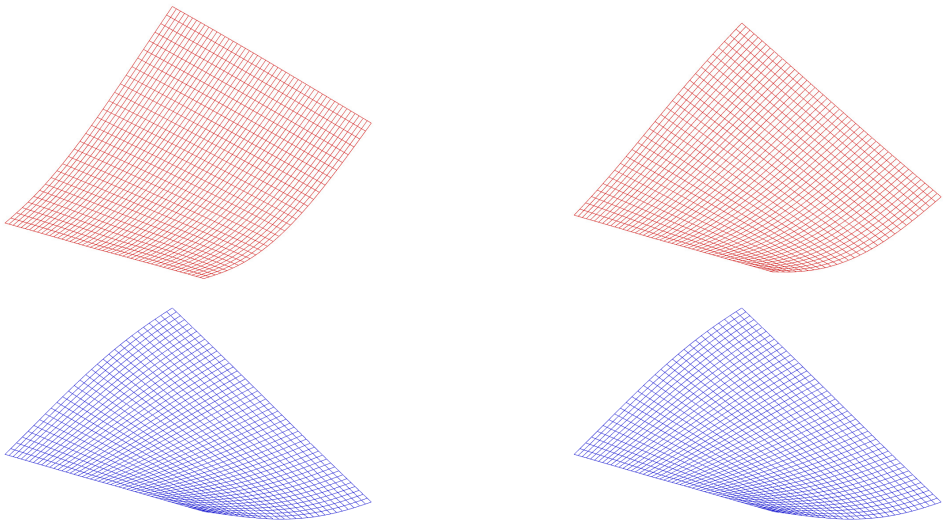

(a) (b)

Figure 3.14. Second structural mode (blue) compared to the second aeroelastic mode (red) of (a) the nominal case, and (b) the $\mu = 24.84$ case for a postulated actuator positioned at 47.5% chord, 2.5% span.

3.4.2 Effects of Natural Frequency

We expect critical velocity to be proportional to structural stiffness and, consequently, natural frequency [4, 17, 18]. The reduced critical velocity normalizes the critical velocity by the corresponding natural frequency, thus removing structural stiffening effects and isolating aeroelastic effects. Fig. 3.15 shows reduced critical velocity across the full range of postulated actuator placements. Here, the reduced velocity decreases with increasing spanwise location, which is opposite of the general trend observed in Fig. 3.7(a). This indicates that, in Fig. 3.7(a), the increase in dimensional critical velocity with increasing spanwise actuator location is entirely due to the added stiffness provided by the change in the placement of the boundary condition, and not due to an increase in the inherent aeroelastic stability of the system. The reduced critical velocity again increases at low chordwise and high spanwise positions near the boundary between flutter and divergence, indicating the system tends to be more aeroelastically stable on the divergence side of the boundary.

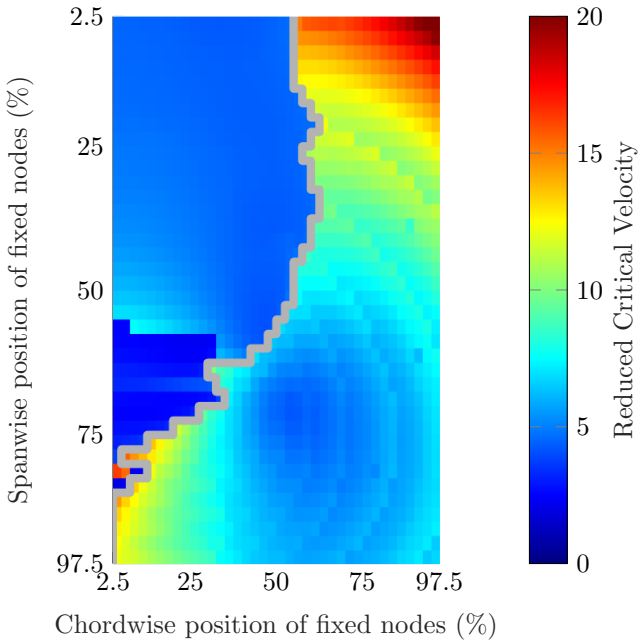

Figure 3.15. Reduced critical velocity as a function of the postulated actuator placement. The gray line overlay shows the boundary between flutter (left) and divergence (right)

Chapter 4

Summary

4.1 Summary of Findings

The aeroelastic instability of a hinged plate with an interior pinned boundary condition is studied using a coupled linear VLM for subsonic potential flow. Instability type, critical velocity, and flutter frequency are reported for a large parameter space, including plate aspect ratio, mass ratio, and various locations and footprint sizes of the interior boundary condition.

As the interior boundary condition is varied, the results reveal the existence of a flutter-divergence boundary. Flutter dominates when the interior boundary condition is placed on the leading-edge side of this boundary, while divergence dominates when it is placed on the trailing-edge side. The chordwise location and shape of the boundary are primarily affected by the plate's aspect ratio, but it may also be affected slightly by the mass ratio or actuator footprint size. The highest critical velocities across all cases seem to appear when the actuator is positioned at a high spanwise (~75%) and a low chordwise (~25%) location. However, the highest reduced critical velocities seem to appear at low span, indicating that the optimal actuator position to achieve the largest dimensional critical velocity is more dependent on structural stiffness than on the coupled aerodynamics. We expect these results to inform preliminary landing gear design by providing a first-order estimate of the optimal actuator position on the door.

4.2 Recommendation for Future Work

Future work could focus on improved modeling. Landing gear doors often experience flow separation near the leading edge that is proportional to the flow speed [4]. The low pressure induced by the flow separation can significantly influence critical velocity predictions. In addition, the actuator strut connecting

the landing gear door to the aircraft likely has a significant effect on the aerodynamics of the surrounding fluid. Fattah [16] states that vortex shedding from the strut is likely the primary source of acoustic noise from aircraft main landing gear. The angle of the landing gear door, the gap between the strut and the door, and the diameter of the strut all affect the system aerodynamics [16]. The inclusion of flow separation effects from the plate leading edge and aerodynamic effects of the strut in an aeroelastic model would enable higher fidelity predictions.

The model presented here uses an idealized, plate-like geometry, while real landing gear doors are often curved to match the contours of the aircraft body (like the door depicted in Fig. 1.1a). Numerical studies considering detailed and realistic landing gear door geometries have been performed [4, 7], but the parameter space is typically much smaller than the space investigated here. A parameter study considering a realistic landing gear door geometry and studying parameters similar to the present work would highlight the differences between the idealized geometry and the high-fidelity geometries used in recent work.

While the presence of flutter does signify a design failure, it does not always result in structural failure. Flutter often manifests as a limit cycle oscillation (LCO), a form of mechanical saturation where the oscillation amplitude is limited by structural nonlinearities. LCO cannot be predicted using the linear methods applied to the present work, but they may be studied by time marching the solution of a linear VLM fluid model coupled to a nonlinear structural model [21,49–51,70,71]. The flow velocity and frequency of a limit cycle oscillation does not in general match the critical velocity or flutter frequency associated with linear flutter for a given configuration. It would be interesting to study the configurations and flow velocities where landing gear doors experience LCO.

Modeling the effects of multiple interior boundary conditions to simulate multiple actuator positions on a landing gear door is also of potential value for design purposes. The inclusion of two or more actuators would significantly change the mode shapes and natural frequencies calculated using a single actuator, which would in turn affect the critical velocities of each configuration. The optimal actuator positions would likely change from the high spanwise, low chordwise location recommended here. Since multiple actuators would likely serve to stiffen the structure even more than a single actuator, a set of design guidelines for landing gear doors with multiple actuator positions would be useful for thin or high aspect ratio doors.

Bibliography

[1] B. K. Morris and R. B. Davis, "Aeroelastic analysis of an idealized landing gear door in subsonic potential flow," Manuscript submitted for publication to Journal of Fluids and Structures, 2020.

[2] Gulfstream, "The gulfstream g650," accessed 2019. http://www.gulfstream.com/aircraft/gulfstream-g650.

[3] Mike James Media, "Boeing 727-100 - wing details and flight control operation," accessed 2020. http://www.mikejamesmedia.com/b727_100_04.html.

[4] E. L. Blades and A. Cornish, "Aeroelastic stability predictions of a business jet landing gear door using high fidelity fluid-structure interaction tools," in *56th AIAA/ASCE/AHS/ASC Structures, Structural Dynamics, and Materials Conference*, p. 0173, 2015.

[5] Federal Aviation Administration, "Electronic code of federal regulations Title 14, Chapter 1, Subchapter C, Part 23 - Airworthiness standards: Normal category airplanes," 2019.

[6] Federal Aviation Administration, "Electronic code of federal regulations Title 14, Chapter 1, Subchapter C Part 25 - Airworthiness standards: Transport category airplanes," 2019.

[7] M. Tomac, A. Rizzit, D. Charbonnier, J. B. Vos, A. Jirasek, S. H. Peng, A. Winkler, A. Allen, G. Wissocq, G. Puigt, J. Dandois, and R. Abarca-Lopez, "Unsteady aero-loads from vortices shed on A320 landing gear door: Cfd compared to flight tests," in *54th AIAA Aerospace Sciences Meeting, 2016, January 4, 2016 - January 8, 2016*, vol. 0 of *54th AIAA Aerospace Sciences Meeting*, American Institute of Aeronautics and Astronautics Inc, AIAA, 2016.

[8] R. Abarca, D. Arenillas, O. Castro, B. Masia, E. Menga, and M. Barth, "Main landing gear door dynamic loads due to unsteady aerodynamics: A predictive and validated methodology," in *16th International Forum on Aeroelasticity and Structural Dynamics, IFASD 2015, June 28, 2015 - July 2, 2015*, International Forum on Aeroelasticity and Structural Dynamics, IFASD 2015, p. Polytec, International Forum on Aeroelasticity and Structural Dynamics (IFASD), 2015.

[9] J. Schwochow, J. Sinske, R. Buchbach, Y. Govers, and R. Abarca-Lopez, "Operational modal analysis of moving aircraft landing gear doors in flight," in *8th International Operational Modal Analysis Conference, IOMAC 2019, May 13, 2019 - May 15, 2019*, 8th IOMAC - International Operational Modal Analysis Conference, Proceedings, pp. 591–603, International Operational Modal Analysis Conference (IOMAC), 2019.

[10] E. Neri, J. Kennedy, P. Eret, and G. J. Bennett, "Aeroacoustic source separation on a full scale nose landing gear featuring combinations of low noise technologies," in *44th International Congress and Exposition on Noise Control Engineering, INTER-NOISE 2015, August 9, 2015 - August 12, 2015*, INTER-NOISE 2015 - 44th International Congress and Exposition on Noise Control Engineering, pp. ADC 40; Institute of Noise Control Engineering of the United States of America (INCE/USA); International Institute of Noise Control Engineering (I–INCE); Korean Society of Noise and Vibration Engineering (KSNVE); NCA, The Institute of Noise Control Engineering of the USA, Inc., 2015.

[11] E. Neri, J. Kennedy, and G. J. Bennett, "Experimental and numerical study of wheel bay cavity noise for full scale nose landing gear," in *23rd AIAA/CEAS Aeroacoustics Conference, 2017, June 5, 2017 - June 9, 2017*, 23rd AIAA/CEAS Aeroacoustics Conference, 2017, American Institute of Aeronautics and Astronautics Inc, AIAA, 2017.

[12] Y. Li, M. G. Smith, X. Zhang, and N. Molin, "Noise sources control of an aircraft landing gear," in *13th AIAA/CEAS Aeroacoustics Conference (28th AIAA Aeroacoustics Conference), May 21, 2007 - May 23, 2007*, 13th AIAA/CEAS Aeroacoustics Conference (28th AIAA Aeroacoustics Conference), American Institute of Aeronautics and Astronautics Inc., 2007.

[13] J. Kennedy, E. Neri, and G. J. Bennett, "The reduction of main landing gear noise," in *22nd AIAA/CEAS Aeroacoustics Conference, 2016, May 30, 2016 - June 1, 2016*, 22nd AIAA/CEAS Aeroacoustics Conference, 2016, American Institute of Aeronautics and Astronautics Inc, AIAA, 2016.

[14] W. Dobrzynski, L. C. Chow, M. Smith, A. Boillot, O. Dereure, and N. Molin, "Experimental assessment of low noise landing gear component design," in *15th AIAA/CEAS Aeroacoustics Conference (30th AIAA Aeroacoustics Conference)*, 15th AIAA/CEAS Aeroacoustics Conference (30th AIAA Aeroacoustics Conference), American Institute of Aeronautics and Astronautics Inc., 2009.

[15] G. J. Bennett, E. Neri, and J. Kennedy, "Noise characterization of a full-scale nose landing gear," *Journal of Aircraft*, vol. 55, no. 6, pp. 2476–2490, 2018.

[16] R. Fattah, Z. Hu, and D. Angland, "Aeroacoustics of a landing gear door," in *19th AIAA/CEAS Aeroacoustics Conference, May 27, 2013 - May 29, 2013*, 19th AIAA/CEAS Aeroacoustics Conference, p. 244, American Institute of Aeronautics and Astronautics Inc., 2013.

[17] H. J. Conyers, E. H. Dowell, and K. C. Hall, "Aeroelastic studies of a rectangular wing with a hole: Correlation of theory and experiment," in *2010 Aerospace Systems Conference*, no. 20100005187, Duke University, 2010.

[18] H. J. Conyers, *The Effect of Wing Damage on Aeroelastic Behavior*. PhD thesis, Duke University, 2009.

[19] J. G. Leishman, "Aerodynamic characteristics of a helicopter rotor airfoil as affected by simulated ballistic damage," Report ADA269206, Army Research Laboratory, 1993.

[20] D. S. Scott, J. C. Westkaemper, A. Sigal, and R. O. Stearman, "The influence of ballistic damage on the aeroelastic characteristics of lifting surfaces," report, Air Force Office of Scientific Research, 1979.

[21] D. Tang, P. Attar, and E. H. Dowell, "Flutter/limit cycle oscillation analysis and experiment for wing-store model," *AIAA Journal*, vol. 44, no. 7, pp. 1662–1675, 2006.

[22] D. Tang and E. H. Dowell, "Flutter and limit-cycle oscillations for a wing-store model with freeplay," *Journal of Aircraft*, vol. 43, no. 2, pp. 487–503, 2006.

[23] P. J. Attar, E. H. Dowell, and D. Tang, "Delta wing with store limit-cycle-oscillation modeling using a high-fidelity structural model," *Journal of Aircraft*, vol. 45, no. 3, pp. 1054–1061, 2008.

[24] A. W. Leissa, "Vibration of plates," Report SP-160, NASA, 1969.

[25] A. E. H. Love and G. H. Darwin, "The small free vibrations and deformation of a thin elastic shell," *Philosophical Transactions of the Royal Society of London. (A.)*, vol. 179, pp. 491–546, 1888.

[26] R. D. Mindlin, "Influence of rotatory inertia and shear on flexural motions of isotropic, elastic plates," *J. App. Mech.*, 1951.

[27] G. B. Warburton, "The vibration of rectangular plates," *Proceedings of the Institution of Mechanical Engineers*, vol. 168, no. 1, pp. 371–384, 1954.

[28] R. Janich, "Die naherungsweise berechnung der eigenfrequenzen von rechteckigen platten bei verschidenen randbedingungen," *Die Bautechnik*, vol. 3, pp. 93–99, 1962.

[29] P. K. Kundu, I. M. Cohen, and D. R. Rowling, *Fluid Mechanics, 6th Edition*. 2015.

[30] S. Farlow, *Partial Differential Equations for Scientists and Engineers*. Dover books on advanced mathematics, Dover Publications, 1993.

[31] F. Roelofs and A. Shams, *CFD—Introduction*, book section 6, pp. 213–218. Woodhead Publishing, 2019.

[32] Y. Nakayama, *Computational Fluid Dynamics*, book section 15, pp. 293–327. Butterworth-Heinemann, 2018.

[33] P. Sagaut and Y.-T. Lee, "Large eddy simulation for incompressible flows: An introduction. scientific computation series," *Applied Mechanics Reviews*, vol. 55, p. 115, 2002.

[34] B. Chaouat, "The state of the art of hybrid rans/les modeling for the simulation of turbulent flows," *Flow, Turbulence and Combustion*, vol. 99, no. 2, pp. 279–327, 2017.

[35] J. Katz and A. Plotkin, *Low-Speed Aerodynamics*. New York: McGraw-Hill Inc., 1991.

[36] J. D. Anderson, *Fundamentals of aerodynamics*. New York: McGraw-Hill Education, 2017.

[37] L. H. Van Zyl, "Robustness of the subsonic doublet lattice method," *Aeronautical Journal*, vol. 107, no. 1071, pp. 257–262, 2003.

[38] L. H. Van Zyl, "Application of the subsonic doublet lattice method to delta wings," *Journal of Aircraft*, vol. 36, no. 3, pp. 609–611, 1999.

[39] L. H. Van Zyl and E. H. Mathews, "Aeroelastic analysis of t-tails using an enhanced doublet lattice method," *Journal of Aircraft*, vol. 48, no. 3, pp. 823–831, 2011.

[40] W. P. Rodden, J. P. Giesing, and T. P. Kalman, "Refinement of the nonplanar aspects of the subsonic doublet-lattice lifting surface method," *Journal of Aircraft*, vol. 9, no. 1, pp. 69–73, 1972.

[41] E. Albano and W. P. Rodden, "A doublet-lattice method for calculating lift distributions on oscillating surfaces in subsonic flows," *AIAA Journal*, vol. 7, no. 2, pp. 279–285, 1969.

[42] W. P. Rodden, P. F. Taylor, and S. C. McIntosh, "Further refinement of the subsonic doublet-lattice method," *Journal of Aircraft*, vol. 35, no. 5, pp. 720–727, 1998.

[43] S. C. Gibbs, "Linear aeroelastic stability of beams and plates in three-dimensional flow," Master's thesis, Duke University, 2012.

[44] J. Murua, R. Palacios, and J. M. R. Graham, "Applications of the unsteady vortex-lattice method in aircraft aeroelasticity and flight dynamics," *Progress in Aerospace Sciences*, vol. 55, pp. 46–72, 2012.

[45] E. A. Kohtanen and R. B. Davis, "Hydroelastic damping of low aspect ratio cantilevered plates," *Journal of Fluids and Structures*, vol. 90, pp. 315–333, 2019.

[46] S. C. Gibbs, A. Sethna, I. Wang, D. Tang, and E. Dowell, "Aeroelastic stability of a cantilevered plate in yawed subsonic flow," *Journal of Fluids and Structures*, vol. 49, pp. 450–462, 2014.

[47] S. C. Gibbs IV, I. Wang, and E. H. Dowell, "Stability of rectangular plates in subsonic flow with various boundary conditions," *Journal of Aircraft*, vol. 52, no. 2, pp. 439–451, 2014.

[48] S. C. Gibbs, I. Wang, and E. Dowell, "Theory and experiment for flutter of a rectangular plate with a fixed leading edge in three-dimensional axial flow," *Journal of Fluids and Structures*, vol. 34, pp. 68–83, 2012.

[49] D. Tang and E. H. Dowell, "Limit cycle oscillations of two-dimensional panels in low subsonic flow," *International Journal of Non-Linear Mechanics*, vol. 37, no. 7, pp. 1199–1209, 2002.

[50] D. Tang, E. H. Dowell, and K. C. Hall, "Limit cycle oscillations of a cantilevered wing in low subsonic flow," *AIAA Journal*, vol. 37, no. 3, pp. 364–371, 1999.

[51] D. Tang, E. H. Dowell, and K. C. Hall, "Limit cycle oscillations of a cantilevered wing in low subsonic flow," *AIAA Journal*, vol. 37, no. 3, pp. 364–371, 1999.

[52] K. C. Hall, R. Florea, and P. J. Lanzkron, "A reduced order model of unsteady flows in turbomachinery," in *ASME 1994 International Gas Turbine and Aeroengine Congress and Exposition*, pp. V005T14A036–V005T14A036, American Society of Mechanical Engineers, 1994.

[53] B. Cao, "Development of reduced unsteady vortex lattice method using proper orthogonal decomposition technique," *AIAA Journal*, vol. 54, no. 1, pp. 366–370, 2016.

[54] A. Kebbie-Anthony, N. A. Gumerov, S. Preidikman, B. Balachandran, and S. Azarm, "Fast multipole accelerated unsteady vortex lattice method based computations," *Journal of Aerospace Information Systems*, vol. 16, no. 6, pp. 237–248, 2019.

[55] B. P. Epps, B. T. Roesler, R. B. Medvitz, Y. Choo, and J. McEntee, "A viscous vortex lattice method for analysis of cross-flow propellers and turbines," *Renewable Energy*, vol. 143, pp. 1035–1052, 2019.

[56] A. T. Nguyen, J.-K. Kim, J.-S. Han, and J.-H. Han, "Extended unsteady vortex-lattice method for insect flapping wings," *Journal of Aircraft*, vol. 53, no. 6, pp. 1709–1718, 2016.

[57] O. Sugar Gabor, A. Koreanschi, and R. M. Botez, "A new non-linear vortex lattice method: Applications to wing aerodynamic optimizations," *Chinese Journal of Aeronautics*, vol. 29, no. 5, pp. 1178–1195, 2016.

[58] M. Parenteau and E. Laurendeau, "Nonlinear frequency-domain solver for vortex lattice method," *AIAA Journal*, vol. 56, no. 6, pp. 2242–2251, 2018.

[59] I. Wang, S. C. Gibbs, and E. H. Dowell, "Flutter of rectangular plates in three dimensional incompressible flow with various boundary conditions: Theory and experiment," in *ASME 2012 International Design Engineering Technical Conferences and Computers and Information in Engineering Conference*, pp. 51–63, American Society of Mechanical Engineers, 2012.

[60] E. H. Dowell, *Aeroelasticity of plates and shells*. Leyden: Noordhoff International, 1975.

[61] K. C. Hall, "Eigenanalysis of unsteady flows about airfoils, cascades, and wings," *AIAA Journal*, vol. 32, no. 12, pp. 2426–2432, 1994.

[62] H. W. Kuhn, "The hungarian method for the assignment problem," *Naval Research Logistics Quarterly*, vol. 2, no. 1-2, pp. 83–97, 1955.

[63] J.-Y. Tinevez, "simpletracker." https://www.mathworks.com/matlabcentral/fileexchange/34040-simpletracker?s_tid=FX_rc1_behav, 2019. Accessed: 2020-02-12.

[64] B. Stanford, P. Beran, and M. Bhatia, "Aeroelastic topology optimization of blade-stiffened panels," *Journal of Aircraft*, vol. 51, no. 3, pp. 938–944, 2014.

[65] A. J. Dodd, K. E. Kadrinka, M. J. Loikkanen, B. A. Rommel, G. D. Sikes, R. C. Strong, and T. J. Tzong, "Aeroelastic design optimization program," *Journal of Aircraft*, vol. 27, no. 12, pp. 1028–1036, 1990.

[66] M. Patil, "Decoupled second-order equations and modal analysis of a general nonconservative system," in *41st Structures, Structural Dynamics, and Materials Conference and Exhibit*, Structures, Structural Dynamics, and Materials and Co-located Conferences, American Institute of Aeronautics and Astronautics, 2000.

[67] R. B. Davis, *Techniques to Assess Acoustic-Structure Interaction in Liquid Rocket Engines*. PhD thesis, Duke University, 2008.

[68] L. Tang and M. P. Paidoussis, "The influence of the wake on the stability of cantilevered flexible plates in axial flow," *Journal of Sound and Vibration*, vol. 310, no. 3, pp. 512–526, 2008.

[69] B. K. Morris, E. A. Kohtanen, and R. B. Davis, "Influence of mixed boundary conditions on the instability of plates in uniform flow," in *International Forum on Aeroelasticity and Structural Dynamics*, 2019.

[70] D. Tang, H. Yamamoto, and E. Dowell, "Flutter and limit cycle oscillations of two-dimensional panels in three-dimensional axial flow," *Journal of Fluids and Structures*, vol. 17, no. 2, pp. 225–242, 2003.

[71] E. Dowell and Y. Weiliang, "Limit cycle oscillation of a fluttering cantilever plate," *AIAA Journal*, vol. 29, no. 11, pp. 1929–1936, 1991.

Appendices

Appendix A

ANSYS Setup Configuration Code

```
! There are 41 rows of nodes, each with 41 nodes. Loop from row 2:40 and column 2:40 (
    reflected in node numbers).
!ALL DIMENSIONS/PROPERIES IN SI UNITS!!

!Code set to display first mode when finished
!Use set,next command followed by pldisp command in GUI to display other mode shapes.
!Use set,list command to display list of natural frequencies

*DIM,nodenumber,,39
nodenumber(1)=176
nodenumber(2)=215
nodenumber(3)=254
nodenumber(4)=293
nodenumber(5)=332
nodenumber(6)=371
nodenumber(7)=410
nodenumber(8)=449
nodenumber(9)=488
nodenumber(10)=527
nodenumber(11)=566
nodenumber(12)=605
nodenumber(13)=644
nodenumber(14)=683
nodenumber(15)=722
nodenumber(16)=761
nodenumber(17)=800
nodenumber(18)=839
nodenumber(19)=878
nodenumber(20)=917
nodenumber(21)=956
nodenumber(22)=995
nodenumber(23)=1034
```

```
nodenumber(24)=1073
nodenumber(25)=1112
nodenumber(26)=1151
nodenumber(27)=1190
nodenumber(28)=1229
nodenumber(29)=1268
nodenumber(30)=1307
nodenumber(31)=1346
nodenumber(32)=1385
nodenumber(33)=1424
nodenumber(34)=1463
nodenumber(35)=1502
nodenumber(36)=1541
nodenumber(37)=1580
nodenumber(38)=1619
nodenumber(39)=1658

*DO,spaniter,1,39,1
*DO,iternumber,1,39,1

!User Inputs

l=1.5           !span [m]
w=0.9           !chord [m]
h=0.001                 !thickness [m]
E=70e9          !Young's modulus [Pa]
rho=2700                !density [kg/m^3]
v=0.3                   !Poisson's ratio [-]

mw_l=10         !Number of mode waves expected along span (used to set mesh density)
mw_w=10         !Number of mode waves expected along chord (used to set mesh density)
epw=4           !number of elements per wave (must be even)
nummodes=9     !number of modes to extract

!Pre-Processor

/PREP7          !enter pre-processor

! Define keypoints

!bottom perimeter

K,1,0,0,0
K,2,w,0,0
K,3,w,l,0
K,4,0,l,0

```

```
!Define lines

L,1,2
L,2,3
L,3,4
L,4,1

!Define number of elements on each line

!set element size along length

LESIZE,1,,,mw_w*epw
LESIZE,2,,,mw_l*epw
LESIZE,3,,,mw_w*epw
LESIZE,4,,,mw_l*epw

!Create Area
AL,1,2,3,4

!Define Element Type

ET,1,SHELL63            !Use Shell63 elements for plate
MP,EX,1,E               !Young's Modulus (Pa)
MP,PRXY,1,v             !Poisson's ratio
MP,DENS,1,rho           !Density of structure (kg/m^3)
R, 1, h                 !Define thickness of plate

!Define Structural Mesh

ASEL,S,,,1              !Select plate area
AATT,1,1,1              !Assign material props, element type, and real constants to area 1
MSHKEY,1
AMESH,ALL

!Set Structural Boundary Conditions

LSEL,S,,,1              !select line 1
NSLL,S,1                !select nodes associated with selected line
D,ALL,UX,0
D,ALL,UY,0
D,ALL,UZ,0
D,ALL,ROTY,0
D,ALL,ROTZ,0
NSEL,S,,,(nodenumber(iternumber)-16)+spaniter !select footprint node elements
! Each call of ESLN, NSLE creates a larger footprint for the ball joint. One call causes a
    5% increase (additive) in chord and spanwise footprint dimensions.
ESLN,S,,1
```

```
NSLE,S,,1

D,ALL,UX,0
D,ALL,UY,0
D,ALL,UZ,0

NSEL,ALL
ESEL,ALL

FINISH                          !Finish pre-processor

!Solution

/SOLU                           !Enter Solution processor

ANTYPE,2
MODOPT,LANB,nummodes                    !Unsymmetric solver, calculate 20 modes up to 1000Hz

MXPAND,nummodes                 !Expand 20 modes

SAVE

SOLVE                           ! Solve the problem
FINISH

! Post-Process

/POST1

!/ANGLE,1,30,XS,1       !Rotate about x-axis for an oblique view of mode shape
!/ANGLE,1,60,YS,1
SET,FIRST       ! Start at first mode
pldisp          !display mode shape

ASEL,,,,1
NSLA,,1

*GET,NNUMMAX,NODE,0,COUNT
*DIM,PRVEC,ARRAY,NNUMMAX,1

*DO,j,1,nummodes,1

*get,natfreq,MODE,j,FREQ
*CFOPEN,platefreqs,dat,,append
*get,pfactor,MODE,j,PFACT
*VWRITE,j,natfreq
(F12.1,10x,F12.4)
```

```
!*ENDDO

*CFOPEN,plate_mode_%iternumber%_%spaniter%_%j%,dat

*DO,i,1,NNUMMAX,1

*get,xpos,NODE,i,LOC,X
*get,ypos,NODE,i,LOC,Y
*get,zpos,NODE,i,LOC,Z
*get,pr,NODE,i,U,Z

*VWRITE,xpos,ypos,zpos,pr
(F12.8,10x,F12.8,10x,F12.8,10x,F12.8)

*ENDDO
SET,NEXT
*ENDDO

*CFCLOS

finish

*DEL,PRVEC
PARSAV,ALL,TSMparams
/CLEAR
PARRES,CHANGE,TSMparams
/prep7

*ENDDO
*ENDDO
```

Appendix B

MATLAB Code

B.1 Main VLM Code

```
%% Inputs
clear all
% Element numbers in chord (S_c) and span (S_s) directions
S_c = 50;
S_s = 60;

% Number of structural modes to be included
nmodes_t = 6;

% Number of structural eigenvalues is nmodes_t*2, and in general (but not
% always) those are the eigenvalues with the highest real part. max_modes sets the
% number of eigenvalues to be stored from the analysis — it is good to play it safe
% and add additional eigenvalues.

max_modes = S_s+nmodes_t*2;

% wake_mult is the ratio of wake columns to chord columns, e.g. number of
% wake columns = wake_mult*S_c.
wake_mult = 0.5;

% Set desired flow speeds to solve for
flowmin = 1;
flowstep = 1;
flowmax = 60;

% Vortex relaxation factor
alpha = 0.992;

% Plate geometry
L_x = 0.9; % Chord length
```

```
L_y = 1.5; % Span length
h = 0.001; % Plate thickness
dx = L_x/S_c;
dy = L_y/S_s;

% Material and fluid properties
E = 70e9; % Young's modulus
mu = 0.3; % Poisson's ratio
rho_s = 2700; % Structural density
rho_f = 1.23; % Fluid density
% Set flow velocity vector
U = flowmin:flowstep:flowmax;

% Degrees of freedom in the overall system matrices
dof = round((1+wake_mult)*(S_c*S_s)+2*nmodes_t);

% Initialize solution matrices
Freq = zeros(max_modes,length(U));
Reall = zeros(dof,length(U));
lambda = zeros(dof,length(U));
Damp = zeros(max_modes,length(U));
Real = zeros(max_modes,length(U));
Imagi = zeros(max_modes,length(U));

chord_pos = 1:39;
span_pos = 1:39;
% Mode shape location
location = ⟨Location of ANSYS Mode Shapes⟩;

%% Analysis
parpool(24)
k = 1; %Change this to match file name. This indicates the spanwise coordinate to study.
for j = 1:length(chord_pos)
        % Call ansys mode shapes and interpolate onto VLM grid.
        [psi,numelem_p,numelem_t] = build_psi_griddata_ansys_IFASD(nmodes_t,S_c,S_s,L_x,L_y,
            location,wake_mult,chord_pos(j),span_pos(k));

        % Build mass and stiffness matrices. Note that M and K are constant with
        % respect to U.
        [M,K] = build_MK_ansys(psi,nmodes_t,mu,E,h,rho_s,numelem_p,S_c,S_s,L_x,L_y);

        parfor i = 1:length(U)
                [kappa,omega,dt] = build_KapOm_ansys(psi,M,K,U(i),rho_f,dy,dx,h,E,L_x,L_y,
                    S_s,S_c,alpha,nmodes_t,wake_mult);

                A = eig(omega,-kappa);

```

```
                lambda = log(A)/dt;
                Reall(:,i) = real(lambda);
                [B I] = sort(Reall(:,i),'descend');
                Imagi(:,i) = imag(lambda(I(1:max_modes)));
                Freq(:,i) = Imagi(:,i)/(2*pi);
                Real(:,i) = real(lambda(I(1:max_modes)));
                Damp(:,i) = -Real(:,i)./sqrt(Imagi(:,i).^2); % New damping definition
        end
        cd(⟨Location of VLM Code⟩);
        csvwrite(sprintf('D_Chordpos%02d_Spanpos%02d.csv',chord_pos(j),span_pos(k)),Damp);
        csvwrite(sprintf('F_Chordpos%02d_Spanpos%02d.csv',chord_pos(j),span_pos(k)),Freq);
end
```

B.2 Structural Mode Shape Interpolation Code

```
function [psi,numelem_p,numelem_t] = build_psi_griddata_ansys_IFASD(nmodes_t,S_c,S_s,L_x,L_y
    ,location,wake_mult,chord_pos,span_pos)

dx = L_x/S_c;
dy = L_y/S_s;

X = dx:dx:(1+wake_mult)*L_x; % length of plate + wake, can experiment with wake length
Y = dy:dy:L_y; % width of wake is same as width of plate

numelem_p = S_s*S_c; % number of plate elements
numelem_w = round(wake_mult*numelem_p); % number of wake elements
numelem_t = numelem_p + numelem_w; % total number of elements

ya = zeros(1,numelem_t);

for i = 1:length(X)
        xa(1+(i-1)*length(Y):i*length(Y))=X(i)-3*dx/4; % left side of horseshoe vortex
        for j = 1:length(Y)
                ya(j+(i-1)*length(Y))=Y(j)-dy; % lower horseshoe vortex
        end
end

% Need to interpolate ANSYS mode shapes to collocation points located at
% x_plate, y_plate on the structure
y = ya+dy/2; % collocation points along y (contains wake elems as well)
x = xa + dx/2; % collocation point along x (contains wake elems)
x_plate = x(1:numelem_p); % contains only structural elems
y_plate = y(1:numelem_p);

cd(location)
```

```
% Mode shape data from ANSYS named in the form '*_chord_pos_span_pos_*.dat'
Files = dir(fullfile(pwd,strcat('*_',num2str(chord_pos),'_',num2str(span_pos),'_*.dat')));

for k = 1:nmodes_t
        Mode = Files(k).name;
        A = importdata(Mode);
        A = round(A,7);
        A = sortrows(A,[2,1]);
        dx_ansys = A(2,1)-A(1,1);
        index = find(A(:,2) ~= A(1,2));
        num_sc = index(1)-1;
        num_ss = length(A)/num_sc;
        dy_ansys = A(index(1),2)-A(1,2);

        t = 0;
        for i = 1:num_ss
                for m = 1:num_sc
                        t = t+1;
                        ANSYS_grid(i,m) = A(t,4);
                end
        end

        % Use gradient operator to find mode shape partial derivatives in x, y, xx,
        % yy, and xy
        [F_x,F_y] = gradient(ANSYS_grid,dx_ansys,dy_ansys);
        [F_xx,F_xy] = gradient(F_x,dx_ansys,dy_ansys);
        [~,F_yy] = gradient(F_y,dx_ansys,dy_ansys);

        t = 0;
        for i = 1:num_ss
                for m = 1:num_sc
                        t = t+1;
                        F_xvec(t,1) = F_x(i,m);
                        F_yvec(t,1) = F_y(i,m);
                        F_xyvec(t,1) = F_xy(i,m);
                        F_xxvec(t,1) = F_xx(i,m);
                        F_yyvec(t,1) = F_yy(i,m);
                end
        end
        % griddata() command interpolates ANSYS mode shapes to given x and y
        % plate coordinates
        psi{k} = zeros(numelem_p,6);
        psi{k}(:,1) = griddata(A(:,1),A(:,2),A(:,4),x_plate,y_plate);
        psi{k}(:,2) = griddata(A(:,1),A(:,2),F_xvec,x_plate,y_plate);
        psi{k}(:,3) = griddata(A(:,1),A(:,2),F_yvec,x_plate,y_plate);
        psi{k}(:,4) = griddata(A(:,1),A(:,2),F_xyvec,x_plate,y_plate);
        psi{k}(:,5) = griddata(A(:,1),A(:,2),F_xxvec,x_plate,y_plate);
```

```
        psi{k}(:,6) = griddata(A(:,1),A(:,2),F_yyvec,x_plate,y_plate);
end

cd(⟨Location of VLM Code⟩)
```

B.3 Aeroelastic Matrix Code

```
function [kappa,omega,dt] = build_KapOm_ansys(psi,M,K,U,rho_a,dy,dx,h,E,L_x,L_y,S_s,S_c,
    alpha,nmodes_t,wake_mult)

X = dx:dx:(1+wake_mult)*L_x; % length of plate + wake
Y = dy:dy:L_y; % width of wake is same as width of plate
dt = dx/U;

numelem_p = S_c*S_s; % number of plate elements
numelem_w = wake_mult*numelem_p; % number of wake elements
numelem_t = numelem_p + numelem_w; % total number of elements

% time step defined as element size divided by U. This way vorticity
% convects exactly the distance of one element length in one time step.

for i = 1:length(X)
        xa(1+(i-1)*length(Y):i*length(Y))=X(i)-3*dx/4; % left side of horseshoe vortex
        for j = 1:length(Y)
                ya(j+(i-1)*length(Y))=Y(j)-dy; % lower horseshoe vortex
        end
end

y = ya+dy/2; % mid element
yb = ya+dy; % upper horseshoe vortex
x = xa + dx/2; % collocation point along x


%% Build Sigma and Xi
% A11: Circulation over wing, time step n+1
% A12: Circulation over wing, time step n
% W11: First column of wake, time step n+1
% W12: First column of wake, time step n
% W21: Columns excluding first and final column in the wake, time step n+1
% W22: Columns excluding first and final column in the wake, time step n
% W31: Last column in the wake, time step n+1
% W32: Last column in the wake, time step n

% Time step n+1 associated with Kappa, time step n is associated
% with omega.
```

```
38
39  A11 = zeros(numelem_p,numelem_t);
40  A12 = zeros(numelem_p,numelem_t);
41
42  for j = 1:numelem_t
43          for i = 1:numelem_p
44                  c1 = -1/(4*pi*(y(i)-ya(j)));
45                  c2 = 1+sqrt((x(i)-xa(j))^2+(y(i)-ya(j))^2)/(x(i)-xa(j));
46                  c3 = 1/(4*pi*(y(i)-yb(j)));
47                  c4 = 1+sqrt((x(i)-xa(j))^2+(y(i)-yb(j))^2)/(x(i)-xa(j));
48                  A11(i,j) = c1*c2+c3*c4;
49          end
50  end
51
52  W11 = zeros(S_s,numelem_t);
53  for i = 1:S_s
54          for j = 1:S_c+1
55                  W11(i,(j-1)*S_s+i) = 1;
56          end
57  end
58
59  % First column of wake
60  W12 = -W11;
61  W12(:,numelem_p+1:end) = 0;
62
63  % Second to second-to-last column of wake
64  numcols = numelem_t/S_s;
65  W21 = [zeros((numcols-S_c-2)*S_s,numelem_p+S_s) eye((numcols-S_c-2)*S_s) zeros((numcols-S_c
        -2)*S_s,S_s)];
66  W22 = -[zeros((numcols-S_c-2)*S_s,numelem_p) eye((numcols-S_c-2)*S_s) zeros((numcols-S_c-2)*
        S_s,2*S_s)];
67
68  % Last column of wake
69  W31 = [zeros(S_s,numelem_t-S_s) eye(S_s)];
70  W32 = -[zeros(S_s,numelem_t-2*S_s) eye(S_s) alpha*eye(S_s)];
71
72  sigma = [A11 ; W11; W21; W31];
73  xi = [A12; W12; W22; W32];
74
75  %% Build Beta (fluid downwash relationships)
76  beta = zeros(numelem_p,2*nmodes_t);
77
78  for j = 1:nmodes_t
79          for i = 1:numelem_p
80                  beta(i,2*j-1) = U*psi{j}(i,2);
81                  beta(i,2*j) = psi{j}(i,1);
82          end
```

```
end

beta = [beta;zeros(numelem_w,2*nmodes_t)];

%% Build C (fluid forcing)

Coeff1 = 1.5*eye(numelem_p);
Coeff2 = -0.5*eye(numelem_p);

for i = 1:numelem_p
        for j = 1:S_c-1
                Coeff1(S_s+(j-1)*S_s+i,i) = 1;
                Coeff2(S_s+(j-1)*S_s+i,i) = -1;
        end
end

Coeff1 = Coeff1(1:numelem_p,1:numelem_p);
Coeff2 = Coeff2(1:numelem_p,1:numelem_p);

C1 = zeros(2*nmodes_t,numelem_t);
C2 = C1;

for i = 1:nmodes_t
        Coeff1_loop = Coeff1;
        Coeff2_loop = Coeff2;
        for j = 1:numelem_p
                Coeff1_loop(j,:) = Coeff1(j,:).*psi{i}(j,1);
                Coeff2_loop(j,:) = Coeff2(j,:).*psi{i}(j,1);
        end
        for j = 1:numelem_p
                C1(i,j) = sum(Coeff1_loop(:,j))*rho_a*dy*U;
                C2(i,j) = sum(Coeff2_loop(:,j))*rho_a*dy*U;
        end
end

%% Structural EOM's

D1 = zeros(2*nmodes_t);
D2 = D1;

for i = 1:nmodes_t
        for j = 1:nmodes_t
                D1(i,2*j-1) = K(i,j)/2;
                D1(i,2*i) = M(i,i)/dt;
                D1(nmodes_t+i,2*i-1) = 1/dt;
                D1(nmodes_t+i,2*i) = -0.5;
                D2(i,2*j-1) = D1(i,2*j-1);
```

```
                D2(i,2*i) = -D1(i,2*i);
                D2(nmodes_t+i,2*i-1) = -1/dt;
                D2(nmodes_t+i,2*i) = -0.5;
        end
end

%% Build Overall Matrices

kappa = [sigma beta; C1 D1];
omega = [xi zeros(size(beta)); C2 D2];
end
```

B.4 Structural Mass and Stiffness Matrix Code

```
function [M,K] = build_MK_ansys(psi,nmodes_t,mu,E,h,rho_s,numelem_p,S_c,S_s,L_x,L_y)

dx = L_x/S_c;
dy = L_y/S_s;

% Compute  bending stiffnesses
D_x = (E*h^3)/(12*(1-mu^2));
D_d = 2*mu*D_x;
D_xy = 2*(1-mu)*D_x;
D_y = D_x;

%% Mass
psi_sqr = zeros(numelem_p,nmodes_t);
for i = 1:nmodes_t
        psi_sqr(:,i) = psi{i}(:,1).^2;
end

for j = 1:nmodes_t
        for i = 1:S_c
                z(1:S_s,i) = psi_sqr(S_s*(i-1)+1:S_s*i,j);
        end
        psi_dxx_int = trapz(z);
        M(j,j) = trapz(psi_dxx_int)*dx*dy*h*rho_s;
end

%% Stiffness

for j = 1:nmodes_t
        for k = 1:nmodes_t
                for i = 1:S_c
```

```
                        psi_dxxdyy(1:S_s,i) = psi{j}(S_s*(i-1)+1:S_s*i,5).*psi{k}(S_s*(i-1)
                            +1:S_s*i,6);
                        psi_dxy(1:S_s,i) = psi{j}(S_s*(i-1)+1:S_s*i,4).*psi{k}(S_s*(i-1)+1:
                            S_s*i,4);
                        psi_dxx(1:S_s,i) = psi{j}(S_s*(i-1)+1:S_s*i,5).*psi{k}(S_s*(i-1)+1:
                            S_s*i,5);
                        psi_dyy(1:S_s,i) = psi{j}(S_s*(i-1)+1:S_s*i,6).*psi{k}(S_s*(i-1)+1:
                            S_s*i,6);
                end
                psi_dxx_int = trapz(psi_dxx);
                psi_dyy_int = trapz(psi_dyy);
                psi_dxxdyy_int = trapz(psi_dxxdyy);
                psi_dxy_int = trapz(psi_dxy);
                K_d(j,k) = trapz(psi_dxxdyy_int)*D_d*dx*dy;
                K_dxy(j,k) = trapz(psi_dxy_int)*D_xy*dx*dy;
                K_dx(j,k) = trapz(psi_dxx_int)*D_x*dx*dy;
                K_dy(j,k) = trapz(psi_dyy_int)*D_y*dx*dy;
        end
end

K = K_dx+K_dy+K_d+K_dxy;
```

B.5 Fluid-Loaded Mode Extraction Code

```
function [] = getLoadedModeShapes(chord,span,U)
%% Inputs
S_c = 50;
S_s = 30;
nmodes_t = 6;
max_modes = S_s+nmodes_t*2;
wake_mult = 0.5;
alpha = 0.992;
L_x = 0.9;
L_y = 1.5;
h = 0.001;
dx = L_x/S_c;
dy = L_y/S_s;
E = 70e9;
mu = 0.3;
rho_s = 2700;
rho_f = 1.23;
dof = round((1+wake_mult)*(S_c*S_s)+2*nmodes_t);

% Initialize solution matrices
Freq = zeros(max_modes,length(U));
```

```
Reall = zeros(dof,length(U));
lambda = zeros(dof,length(U));
Damp = zeros(max_modes,length(U));
Real = zeros(max_modes,length(U));
Imagi = zeros(max_modes,length(U));
Vecs = zeros(dof,max_modes,length(U));

% Mode shape location
location = ⟨Location of ANSYS Modes⟩;

%% Analysis
[psi,numelem_p,numelem_t] = build_psi_griddata_ansys_IFASD(nmodes_t,S_c,S_s,L_x,L_y,location
    ,wake_mult,chord,span);
[M,K] = build_MK_ansys(psi,nmodes_t,mu,E,h,rho_s,numelem_p,numelem_t,S_c,S_s,L_x,L_y);
[kappa,omega,dt] = build_KapOm_ansys(psi,M,K,U,rho_f,dy,dx,h,E,L_x,L_y,S_s,S_c,alpha,
    nmodes_t,wake_mult,0);

% Generate left and right eigenvectors in addition to eigenvalues
[phiR,A,phiL] = eig(omega,-kappa,'vector');

lambda = log(A)/dt;

Reall(:,i) = real(lambda);
[B I] = sort(Reall(:,i),'descend');
Imagi(:,i) = imag(lambda(I(1:max_modes)));
Freq(:,i) = Imagi(:,i)/(2*pi);
Real(:,i) = real(lambda(I(1:max_modes)));
Damp(:,i) = -Real(:,i)./sqrt(Imagi(:,i).^2);

%% Extract Loaded Mode Shapes
% Sort raw eigenvectors and discrete eigenvalues according to
% post-proc sorting
phiR = phiR(:,I(1:max_modes));
A = A(I(1:max_modes));

% Delete all data associated with a natural frequency of 0.
I = (~isinf(Damp));
phiR = phiR(:,I);
A = A(I);
Freq = Freq(I);
Damp = Damp(I);

% Assemble real basis from complex eigenvectors according to
% multiphysis eq. 2.129
newphiR = zeros(size(phiR));
for l = 1:length(phiR(1,:))/2
```

```
        newphiR(:,(2*l-1):(2*l)) = [real(phiR(:,(2*l-1)))-(real(A(2*l-1))/imag(A(2*l-1)))*
            imag(phiR(:,(2*l-1))),(1/imag(A(2*l-1)))*imag(phiR(:,(2*l-1)))];
end
% Trim unnecessary rows (associated with Gamma and qdot)
phiComplex = newphiR(end-2*nmodes_t+1:2:end,:);

% Delete columns associated with eta
phiComplex = phiComplex(:,1:2:end);
A = A(1:2:end);
Freq = Freq(1:2:end);
Damp = Damp(1:2:end);

% Sort mode shapes according to frequency
[Freq,I] = sort(Freq,'ascend');
Damp = Damp(I);
A = A(I);
phiComplex = phiComplex(:,I);

% Generate new aeroelastic mode shapes as weighted sum of in-vacuo
% modes
psiAero = cell(1,nmodes_t);
for l = 1:nmodes_t
        psiMat(:,l) = psi{l}(:,1);
end
psiMat = psiMat*phiComplex;
for l = 1:nmodes_t
        psiAero{l} = psiMat(:,l);
end

csvwrite(sprintf('LoadedModes_Chordpos%02d_Spanpos%02d.csv',chord,span),psiMat);
```